ENGINEERING.
IMPACTO CIENTÍFICO EDITORA

USING A HIGH-RESOLUTION SCHEME IN A FINITE VOLUME CODE TO SIMULATE SUPERSONIC COMPRESSIBLE FLUID FLOWS IN NOZZLES

USO DE UM ESQUEMA DE ALTA RESOLUÇÃO EM UM CÓDIGO DE VOLUMES FINITOS PARA SIMULAR ESCOAMENTOS DE FLUIDOS COMPRESSÍVEIS SUPERSÔNICOS EM BOCAIS

USO DE UN ESQUEMA DE ALTA RESOLUCIÓN EN UN CÓDIGO DE VOLÚMENES FINITOS PARA SIMULAR FLUJOS DE FLUIDOS COMPRESIBLES SUPERSÓNICOS EN TOBERAS

https://doi.org/10.56238/edimpacto2025.086-004

Pablo Manolo Zych Langhinoti[1], Francisco Augusto Aparecido Gomes[2], João Biesdorf[3], Rômel da Rosa da Silva[4]

ABSTRACT

In this work, numerical simulations were carried out for supersonic compressible fluid flows inside geometries related to rocket engines — specifically, convergent-divergent nozzles. To investigate the flow behavior within these nozzles, the Euler and Navier–Stokes equations were numerically solved. The simulations were performed using the HYNE2D code, which is based on the finite volume method and implemented in the Fortran 2003 programming language. The HYNE2D code includes numerous convective and viscous flux functions and performs time discretization either explicitly or implicitly on unstructured meshes. The simulations based on the Euler equations aimed to verify the numerical accuracy of the code through the physical consistency of the results. For the Navier–Stokes equations, the objective was to assess whether the high-resolution method accurately captures shock and expansion waves while reproducing a Mach number equal to one at the nozzle throat. Additionally, the study analyzed the conversion of thermal energy into kinetic energy in bell-shaped and conical nozzles. The results obtained in this work were compared with related literature, showing good accuracy.

Keywords: Convergent-Divergent Nozzles. Supersonic Nozzles. Finite Volume Method. High-Resolution Scheme. Roe Scheme.

[1] Mechanical Engineer. Universidade Tecnológica Federal do Paraná. E-mail: pablo_langhinoti@hotmail.com
Lattes: http://lattes.cnpq.br/7050737820691906
[2] Dr. of Aeronautical and Mechanical Engineering. Universidade Tecnológica Federal do Paraná.
E-mail: franciscogomes@utfpr.edu.br Orcid: https://orcid.org/0000-0001-6204-1439
Lattes: http://lattes.cnpq.br/4960562897145659
[3] Dr. of Mathematics. Universidade Tecnológica Federal do Paraná. E-mail: jbiesdorf@utfpr.edu.br
Orcid: https://orcid.org/0000-0002-9261-7280 Lattes: http://lattes.cnpq.br/9789976538941920
[4] Dr. of Mathematics. Universidade Tecnológica Federal do Paraná. E-mail: romelsilva@utfpr.edu.br
Orcid: https://orcid.org/0000-0003-3206-9320 Lattes: http://lattes.cnpq.br/3804309368611422

RESUMO
Neste trabalho, foram realizadas simulações numéricas de escoamentos de fluidos compressíveis supersônicos em geometrias relacionadas a motores de foguete — especificamente, bocais convergentes-divergentes. Para investigar o comportamento do escoamento nesses bocais, as equações de Euler e de Navier–Stokes foram resolvidas numericamente. As simulações foram executadas utilizando o código HYNE2D, que é baseado no método de volumes finitos e implementado na linguagem de programação Fortran 2003. O código HYNE2D inclui diversas funções de fluxo convectivo e viscoso e realiza a discretização temporal de forma explícita ou implícita em malhas não estruturadas. As simulações baseadas nas equações de Euler tiveram como objetivo verificar a precisão numérica do código por meio da consistência física dos resultados. Para as equações de Navier–Stokes, o objetivo foi avaliar se o método de alta resolução captura adequadamente as ondas de choque e expansão, além de reproduzir um número de Mach igual a um na garganta do bocal. Além disso, o estudo analisou a conversão de energia térmica em energia cinética em bocais do tipo sino (bell-shaped) e cônicos. Os resultados obtidos neste trabalho foram comparados com a literatura relacionada, apresentando boa precisão.

Palavras-chave: Bocais Convergentes-divergentes. Bocais Supersônicos. Método de Volumes Finitos. Esquema de Alta Resolução. Esquema de Roe.

RESUMEN
En este trabajo se realizaron simulaciones numéricas de flujos de fluidos compresibles supersónicos dentro de geometrías relacionadas con motores cohete —específicamente, toberas convergentes-divergentes—. Para investigar el comportamiento del flujo dentro de estas toberas, se resolvieron numéricamente las ecuaciones de Euler y de Navier–Stokes. Las simulaciones se llevaron a cabo mediante el código HYNE2D, el cual está basado en el método de volúmenes finitos y fue implementado en el lenguaje de programación Fortran 2003. El código HYNE2D incluye numerosas funciones de flujos convectivos y viscosos, y realiza la discretización temporal de forma explícita o implícita en mallas no estructuradas. Las simulaciones basadas en las ecuaciones de Euler tuvieron como objetivo verificar la precisión numérica del código a través de la consistencia física de los resultados. Para las ecuaciones de Navier–Stokes, el objetivo fue evaluar si el método de alta resolución captura con precisión las ondas de choque y de expansión, además de reproducir un número de Mach igual a uno en la garganta de la tobera. Adicionalmente, el estudio analizó la conversión de energía térmica en energía cinética en toberas de campana y cónicas. Los resultados obtenidos en este trabajo fueron comparados con la literatura relacionada, mostrando una buena precisión.

Palabras clave: Toberas Convergentes-divergentes. Toberas Supersónicas. Método de Volúmenes Finitos. Esquema de Alta Resolución. Esquema de Roe.

1 INTRODUCTION

Analytical solutions usually present satisfactory results, however they are quite limited in practical cases, because they require simpler study geometries and, generally, it is necessary to adopt several conditions to simplify the physical model, such as constant physical properties, aiming at the elimination of variables and making the calculation feasible (LAROCA, 2000).

Experimental analyses are carried out with the help of test benches, or wind tunnels, in the case of flows around aerodynamic geometries, where environments and conditions similar to real situations are reproduced and flow characteristics are measured through wisely positioned sensors. The main limiting factor in this type of experiment is the costs, which are usually quite high in more complex cases (LAROCA, 2000).

Computer-aided numerical simulations have been very important for understanding physical phenomena in flow analysis since the 1970s. With the advancement in computational power, computer simulations have come to play a key role in the analysis of physical problems involving fluid flows. offer a less costly option in obtaining results in flow analysis. The main tools for obtaining these results are based on Computational Fluid Dynamics (CFD). In CFD, more diverse problems can be studied, such as flows in the arteries of the human body, around buildings, with chemical reactions, in studies of pollutant dispersion in the atmosphere and even in weather forecasts (TU et al., 2018; HIRSH, 2007).

The study of the behavior and consequences of internal flow in geometries of interest to engineering is a fundamental part of equipment projects such as: heat exchangers, compressors, pumps, internal combustion engines. In a complementary way, the understanding of flows around aerodynamic geometries are characteristic of car, motorcycle, airplane and rocket designs (LAROCA, 2000). Knowledge in the aerospace area also plays a fundamental role in history. As an example, we have the space race during the historical period called the Cold War (MOURÃO, 1999).

The development of aerospace technologies represents a milestone for the scientific maturation of a nation, (LORENA, 2014). Above all, in strategic applications, such as the flight of aerospace vehicles through the Earth's atmosphere towards space, telecommunications, meteorological data and remote sensing. From aerospace flight, "rockets evolved from simple gunpowder tubes to powerful vehicles capable of launching a spacecraft towards the galaxies" (NASA, 2009).

The design of a rocket involves basic principles from several areas, such as: mechanical design, thermodynamics and chemistry (SUTTON; BIBLARZ 2000). Also a fundamental part related to rockets is the knowledge of the behavior of fluids, both on the

outside and inside parts of a rocket. Of great prominence and fundamental importance in the rockets, the tomb is mentioned. This component represents total importance in the design of a rocket, as it is responsible for configuring the thrust necessary for the ascending flight of the rocket (SUTTON; BIBLARZ 2000).

According to Taillandier (2006), there are four basic elements of a rocket: the payload, the propellant reservoir, the combustion chamber and finally, the nozzle. The payload depends on the individual objective of the rocket, with the following options: a crew, a satellite, weapons, among others. The propellant reservoir is the volume destined for fuel that will enable the launch and upward flight of the rocket. The combustion chamber is the place where the combustion reactions of the propellant occur, as a result of which there are gases at high temperatures and pressures.

The mouthpiece, also known as the mouthpiece, is the main focus of this study. According to Miraglia (1995, p.13) "The nozzle converts and directs the combustion gases generated at a high temperature (T), high pressure (p) and low speed (Mach number), through an isoentropic expansion, in a flow of gases at lower temperature and pressure and at high supersonic speeds". We can observe these characteristics in the diagram in Fig. 1.

Figure 1

Properties and Mach number in the nozzle

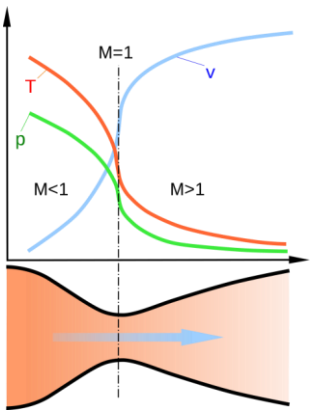

Source: BARROS, José E. Mautone. (2017).

The concept of sonic velocity is a relationship with the speed of sound (c). The Mach number (M) is the division of the flight speed (u) by the local speed of sound (c). A Mach number less, equal to or greater than 1, corresponds respectively to a so-called subsonic, sonic and supersonic speed. The Mach number is calculated as

$$M \equiv \frac{u_\infty}{c}. \qquad (1)$$

To reach supersonic speeds, combustion gases must pass through a combination of ducts called convergent-divergent nozzles. In the convergent mouthpiece, the speed is limited to the sonic speed, which can occur in the throat of the mouthpiece. The divergent section must be attached after the throat and makes it possible to reach supersonic speeds. (ÇENGEL AND BOLES, 2006), (FOX, 2009). Fig. 2 identifies the parts of a nozzle.

Figure 2

Configuration of a convergent-divergent nozzle

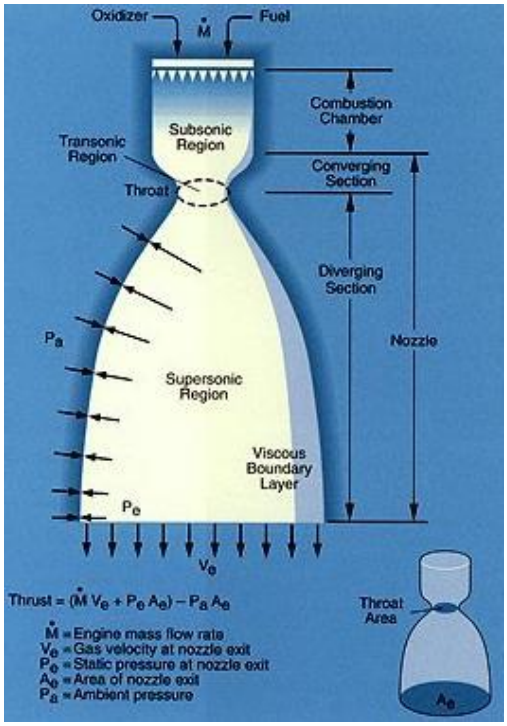

Source: MAKRIS, K. (https://www.k-makris.gr/nozzle-design/).

The convergent section of the nozzle is not a critical region for high performance. Therefore, different radii, angle of convergence, contour of the geometry or entrance of the nozzle present satisfactory results. The contour of the throat is also not critical. The pressure gradient in these two regions is high and the flow adheres to the wall. The big difference between the nozzles is the divergent section (SUTTON; BIBLARZ 2000). In the throat region, Fig. 2, the Mach number is equal to one.

Swedish inventor Gustaf de Laval, around 1888, developed the nozzle containing a convergent section followed by a divergent section, with the aim of increasing the efficiency of a steam turbine. That is why they are known as convergent-divergent mouthpiece or Laval mouthpiece. Over time, variations of these mouthpieces have emerged, but based on the same principle (RADTKE, 2014). These variations can be classified into three main types: conical, bell, and parabolic, as illustrated in Fig. 3.

Figure 3

Types of nozzles: (a) conical profile; (b) bell profile; (c) parabolic profile.

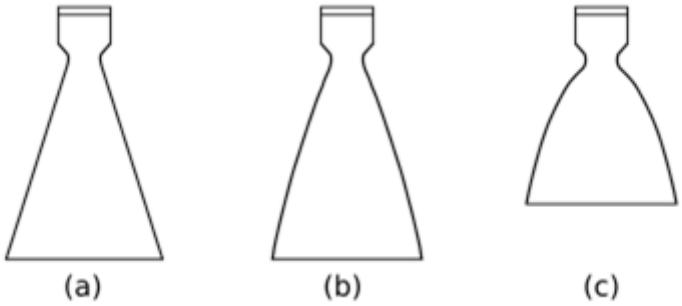

Source: RADTKE, Jonas Joacir. (2014, p.23)

The conical nozzle is the oldest and perhaps the simplest, its inclination is 15° on the wall of the convergent-diverging section and its manufacture is considerably easy and it is still used in small nozzles (SUTTON; BIBLARZ, 2000). In contrast to its relative simplicity, the conical nozzle often has unacceptable performance losses due to the large divergence of flows. These losses can be mitigated by the use of contours that make the flow of gases return to the axial direction of output. This is the purpose of the use of circular and parabolic arcs (HOFFMAN, 1987).

For this reason, RAO (1958) proposed a bell-shaped divergent section nozzle that has a higher thrust coefficient compared to a conical profile nozzle of the same length and area ratio. The bell-shaped nozzle is probably the most common geometry today. It has a high opening angle (20 to 50°) just after the throat and the same angle in the exit section, which should generally be less than 10° (SUTTON; BIBLARZ, 2000).

From the moment the supersonic speed is reached, there is the possibility of the formation of shock waves and/or expansion fans. The shock wave occurs due to a variation in the direction of flow with a positive angle in relation to the plane. While expansion fans form when the flow meets a negative deflection. This makes it possible to adapt the flow through the channel, where, for example, the flow immediately adjacent to the walls must be parallel to them. (ANDERSON, 2003), Fig. 4.

Figure 4

Shock wave and expansion fan

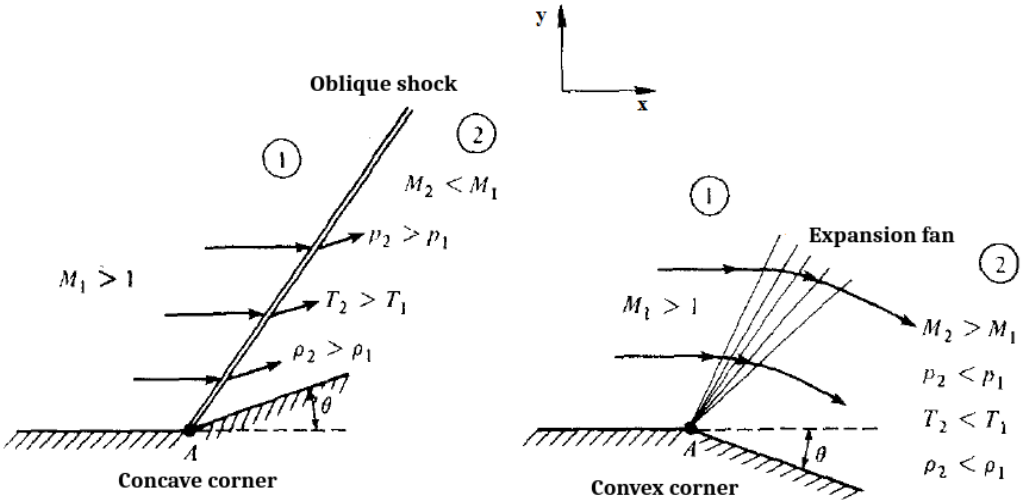

Source: Modified - Anderson J. D. (2003).

The simulations performed in the present work were executed in the code ***HYNE2D*** (Hypersonic Nonequilibrium Two-dimensional solver), (GOMES, 2012). The code ***HYNE2D*** simulates two-dimensional compressible fluid flow, considering the Navier-Stokes and Euler equations, for an ideal gas model or in thermochemical non-equilibrium. It was implemented in the Fortran 2003 programming language, employs discretization via the finite volume method in unstructured meshes and high-order precision in discretizations in space and time. The solver has several methods for calculating convective flow and methods for advancing in explicit and implicit time.

The present work aims to verify the physical coherence of the results in the application of a high-order precision method, in high-speed flow of compressible fluid inside nozzles. Geometry commonly used in rocket engines. Simulations were performed in non-viscous and viscous flows, Euler and Navier-Stokes equations, respectively.

2 MATHEMATICAL FORMULATION OF THE PHYSICAL PROBLEM

The mathematical formulation of the physical problem is applied to the compressible fluid under the continuum hypothesis and conconstant physical properties, represented by the two-dimensional Navier-Stokes equations in Cartesian coordinates, written in the form

$$\frac{\partial}{\partial t}\int_{\Omega} \vec{Q}\, d\Omega + \oint_{\partial\Omega}\left(\overrightarrow{F_c} - \overrightarrow{F_v}\right) dS = 0, \tag{2}$$

Where:

$$\vec{Q} = \begin{Bmatrix} \rho \\ \rho u \\ \rho v \\ \rho E \end{Bmatrix} \text{and} \vec{F_c} = \begin{Bmatrix} \rho V \\ \rho u V + n_x p \\ \rho v V + n_y p \\ \rho H V \end{Bmatrix} \vec{F}_v = \begin{Bmatrix} 0 \\ n_x \tau_{xx} + n_y \tau_{xy} \\ n_x \tau_{yx} + n_y \tau_{yy} \\ n_x \Theta_x + n_y \Theta_y \end{Bmatrix} \quad \Theta_x = u\tau_{xx} + v\tau_{xy} + k\frac{\partial T}{\partial x}, \quad \Theta_y = u\tau_{yx} + v\tau_{yy} + k\frac{\partial T}{\partial y}. \tag{3}$$

The term defines the vector of conserved variables, where is the density, ($\vec{Q}\rho u,v$) represent the velocity components in the Cartesian coordinates (x, y), respectively, E is the total energy per unit volume, H the total enthalpy, (n_x, ny) are the components of the normal vector in the face of the control volume, Fig. 4, $\vec{n}V$ is the velocity projected in the normal direction on the face of the control volume, is the tension tensor of viscous and k is the thermal conductivity of the material, and are respectively the convective and viscous flows, (BLAZEK, 2006).$\tau_{ij}\overrightarrow{F_c}\overrightarrow{F_v}$

Navier–Stokes equations can be simplified by obtaining equations known as Euler equations. In Euler's equations, viscous flux is completely disregarded. This effect is assumed when the interest is purely centered on the observation of the flow behavior in relation to the interactions between shock waves and expansion waves, (BLAZEK, 2006).

3 NUMERICAL METHODOLOGY

The domain of the solution in a numerical model is represented by the computational mesh. In this work, the Navier-Stokes, Eq. (1), were discretized by the finite volume method in unstructured meshes. In the representation of the triangular control volume (Ωi) in Fig. 4, the two-dimensional projections of the convective and viscous flows on each face of the control volume (Γk|) are indicated with reference to the direction of the normal vector to the face of the control volume, Fig. 5.

Figure 5

Representation of a Control Volume

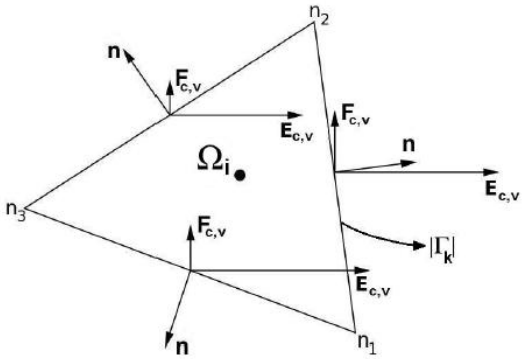

Source: GOMES (2012, p.99)

The discretization of Navier-Stokes equations, Eq. (2), can be performed considering an arbitrary control volume Ωi, Fig. 5, resulting in

$$\frac{d\vec{Q}_i}{dt} = \vec{R}_i, \tag{4}$$

Where:

is the solution residue, $\overrightarrow{R_i}$

$$\vec{R}_i = \frac{-1}{|\Omega_i|}\sum_{k=1}^{N_f} \vec{f}_{n_k}(\vec{Q}_k)|\Gamma_k|, \tag{5}$$

Where:

represents the projected numerical flow in the normal direction on the edge $\overrightarrow{f_{n_k}}(\overrightarrow{Q_k}) = (\vec{F}_{Cn_k} - \vec{F}_{Vn_k})k$.

3.1 CONVECTIVE FLOW

The nonlinear hyperbolic nature of convective flow equation systems implies oscillations of the interfaces of the control volumes in the flow calculation. To minimize such oscillations, it is desirable to opt for numerical methods called upwind schemes. These schemes are widely used in aerodynamics studies, with emphasis on simulations of supersonic and hypersonic flows. To solve the discontinuities in the interfaces of the control volumes, the Riemann problem is used (TORO, 2009).

The exact solution to the Riemann problem is possible and uses values of the properties of the two control volumes that share the same edge, however it requires an

iterative process, which represents a high computational cost. Approximate solutions that do not require iterative methods are used for faster results.

The code ***HYNE2D*** It has numerous flow functions for the calculation of convective flow. In the present work, the Flow Difference Separation Method (*Flux Difference Sppliting* – FDS) of Roe, (ROE, 1981), (BLAZEK, 2006), (NISHIKAWA; KITAMURA, 2008).

3.2 VISCOUS FLOW

To perform the calculation of viscous flow, primitive flow variables such as velocity and temperature are required at the centroid and at the nodes that form each edge. With this, it is possible to calculate the partial derivatives of the Navier-Stokes equations in viscous terms (GOMES, 2012), represented in equations (31), (32) and (33).

The ***HYNE2D*** code calculates viscous flow in a similar way to the work of JAWAHAR and KAMATH (2000), where the gradients at the edges are calculated from a weighted average of a set of gradients calculated in "control sub-volumes" on the edge.

3.3 HIGH-ORDER METHOD

In the flow of compressible fluid, precision high-order methods are also known as high-resolution methods, (VAN LEER, 2003). The code ***HYNE2D*** has a high-order precision scheme based on linear polynomials (BLAZEK, 2006) and (KITAMURA AND SHIMA, 2012), such as

$$q_{ij} = q_i + \phi_i \nabla q_i \cdot (r_{i,j} - r_i), \tag{6}$$

Where:

q_{ij}: are the variables at the interface of the volumes;

q_i: is the value extrapolated to the center of the volume;

∇q_i: are gradients;

r_i: is the distance from the center of the volume to its interface .$r_{i,j}$

The term ϕi represents the limiter of the high-order precision scheme, used to control numerical oscillations, (KITAMURA AND SHIMA, 2012).

3.4 BOUNDARY CONDITIONS

In ***the HYNE2D*** code, boundary conditions are applied using a data structure stored in memory bins only for the calculation of boundary conditions. To implement this data structure, ghost cells (gh) are used. Phantom volumes are dummy control volumes used to

establish calculations related to boundary conditions. Therefore, they are not physically represented in the solution domain (GOMES, 2012).

In Fig. 6 a phantom volume with dashed lines is presented. The term represents an internal control volume of the fabric, while it represents the phantom volume.$\Omega_i \Omega_{gh}$

Figure 6

Representation of a phantom volume

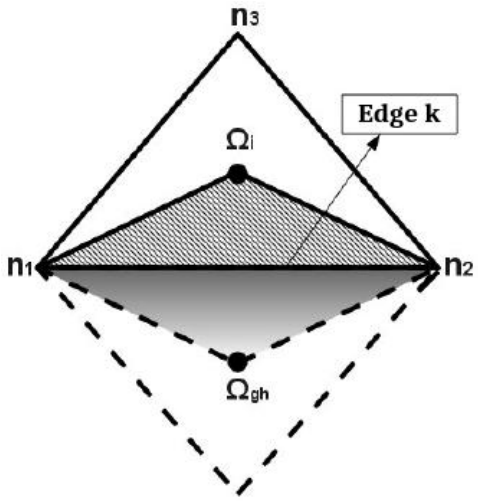

Source: Gomes (2012 p.150).

3.4.1 Boundary Conditions for Convective Term

In this term, the calculation of the convective flow is performed with Euler's system of equations, (BLAZEK, 2006).

3.4.1.1 Wall boundary condition and symmetry

The calculation of boundary conditions for wall and symmetry is implemented in the same way. It is necessary to cancel out the influences of the normal velocity component on the wall, , (HIRSCH, 1991). For this, the equations for the following velocity are used in phantom volumes,$\vec{V}.\vec{n}_w = 0$

$$u_{gh} = (1 - 2n_{wx}^2)u_i - 2n_{wx}n_{wy}v_i,$$

$$u_{gh} = -2n_{wx}n_{wy}u_i + (1 - 2n_{wx}^2)u_i. \quad (7)$$

In the previous relations, the sub-indices *i* are assigned to the terms that represent values within the computational domain. The other properties on phantom volumes are obtained from the internal values of the computational domain, i.e.,

$$\rho_{gh} = \rho_i, \quad (8)$$

$$e_{gh} = e_i. \quad (9)$$

3.4.1.2 Input Boundary Condition

The properties of the flow input are provided by the user and allocated directly to the phantom volumes. Since the variables are conserved at the input, we have$\vec{Q}_e$

$$\vec{Q}_{gh} = \vec{Q}_e. \quad (10)$$

3.4.1.3 Output Boundary Condition

The simulated flows in this work are supersonic, which implies a supersonic output condition. The properties of the output phantom cells are approximated by the internal values of the computational domain,

$$\vec{Q}_{gh} = \vec{Q}_i. \quad (11)$$

3.4.2 Boundary Conditions for Viscous Terms

The viscous terms imply the calculation of the viscous flow with the Navier-Stokes system of equations, (BLAZEK, 2006).

3.4.2.1 Wall Boundary Conditions

For the viscous flow on the wall, the velocity must be equal to zero and the other properties are extrapolated with the internal values of the computational domain, so the relationships are used

$$u_{gh} = -u_i, \quad (12)$$

$$u_{gh} = -v_i, \quad (13)$$

$$\rho_{gh} = \rho_i, \quad (14)$$

$$e_{gh} = e_i. \quad (15)$$

3.4.2.2 Entry boundary conditions

The properties of the flow input are provided by the user and allocated directly to the phantom volumes. Since the variables are conserved at the input, we have$\vec{Q}_e$

$$\vec{Q}_{gh} = \vec{Q}_e. \tag{16}$$

3.4.2.3 Exit boundary conditions

The output boundary conditions, for viscous cases, are obtained by extrapolating from zero order the values belonging to the computational domain, then

$$\vec{Q}_{gh} = \vec{Q}_i. \tag{17}$$

3.4.2.4 Symmetry boundary conditions

This condition is defined in an analogous way to the wall condition for non-viscous flow, , (BLAZEK, 2006).

3.5 DISCRETIZATION IN TIME

The time-discretization method implemented in the ***HYNE2D*** code is known as Runge-Kutta TVD of third-order precision (RK-TVD3) and three steps, (GOTTLIEB; SHU, 2009), (TITAREV; TSOUTSANIS; DRIKAKIS, 2010),

$$\bar{\vec{Q}}^{n+\frac{1}{3}} = \bar{\vec{Q}}^{n} + \Delta t R\left(\bar{\vec{Q}}^{n}\right),$$

$$\bar{\vec{Q}}^{n+\frac{2}{3}} = \frac{3}{4}\bar{\vec{Q}}^{n} + \frac{1}{4}\bar{\vec{Q}}^{n+\frac{1}{3}} + \frac{1}{4}\Delta t R\left(\bar{\vec{Q}}^{n+\frac{1}{3}}\right), \tag{18}$$

$$\bar{\vec{Q}}^{n+1} = \frac{1}{3}\bar{\vec{Q}}^{n} + \frac{2}{3}\bar{\vec{Q}}^{n+\frac{2}{3}} + \frac{2}{3}\Delta t R\left(\bar{\vec{Q}}^{n+\frac{2}{3}}\right).$$

The time step () is calculated for each control volume via the expressionΔt_i

$$\Delta t_i = (CFL)\frac{h_i}{|v_i| + c_i}. \tag{19}$$

At Eq. (18), CFL is the Courant-Friedrichs-Lewy number that provides stability in the method of advancing time, (LEVEQUE, 2002), (HIRSCH, 2007). The characteristic length of

the mesh represented by , is the local velocity of sound and is the magnitude of the velocity at the i-th control volume that is calculated by the norm taking into account its components on the Cartesian axes .$h_i c_i |v_i||v_i| = (\sqrt{u^2 + v^2})_i$

3.6 DESCRIPTION OF THE METHODOLOGY

The performance of this work aims at the numerical analysis of fluid flows at high speeds within specific geometries. Therefore, initially, a study was made on such flows and their characteristics, and articles, theses and materials that could be used as reference were sought. From this, cases were chosen for simulation, which implies three steps:

(i) Development of the geometries of interest and the creation of a mesh. The *GMSH software (GEUZAINE and REMACLE, 2009) was used;*

(ii) To run the simulation, the source code ***HYNE2D was used*** through compilation with the *Gfortran software (GNU PROJECT, 2015);*

(iii) The preparation of diagrams for analysis of the results was done with the *Paraview software (AHRENS et al., 2015).*

4 RESULTS

In the simulated cases in the present work, two-dimensional geometries and unstructured meshes with triangular volumes were used. As a stopping criterion, a residue of the order of *10-12 was used*, *having as reference, the equation of conservation of the mass.*

4.1 NON-VISCOUS FLOW

The non-viscous flow is simulated using Euler's equations. This formulation allows us to observe physical phenomena such as shock waves and expansion fans with a relatively low computational cost. Results of this study will be compared with data found in the literature.

4.1.1 Circular Bump

The geometry used in this case consists of a channel with a *bump* thickness of 4% of the length of the rope, (AKDEMIR, 2010). Fig. 7 shows the mesh used in this simulation, containing 2200 control volumes and 1175 nodes.

Figure 7

Mesh for the circular bump case

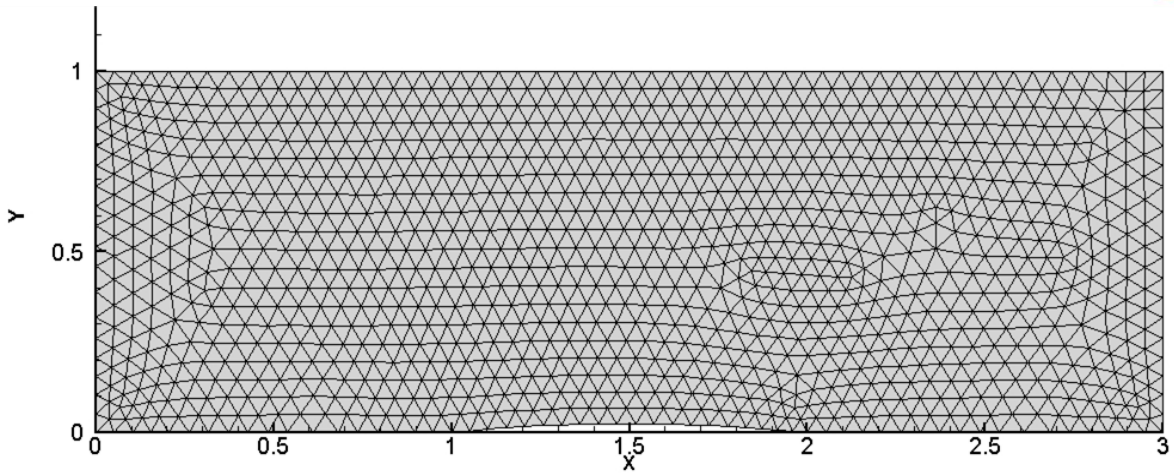

Source: The author.

The identification of the boundary conditions of the entrance, exit and wall are indicated in Fig. 8. To perform this simulation, the following initial condition is assumed

$$\frac{P}{P_o} = 3{,}1822 \qquad (20)$$

$$\frac{T}{T_o} = 1{,}392 \qquad (21)$$

With these relationships we have the Mach number of the flow equal to 1.4, (AKDEMIR 2010).

The expected result is the representation of the shock waves that are formed due to the change in geometry caused by *the bump,* which changes the behavior of the flow. The first shock wave should form at the beginning of the circular section. When it meets the top wall, the shock wave should be reflected and crosses the second shock wave formed just after the *bump.* The two shock waves must merge before the canal exits, Fig. 8. A drop in Mach number values and an increase in pressure and density in the region are expected after the shock wave.

Figure 8

Expected result for Bump

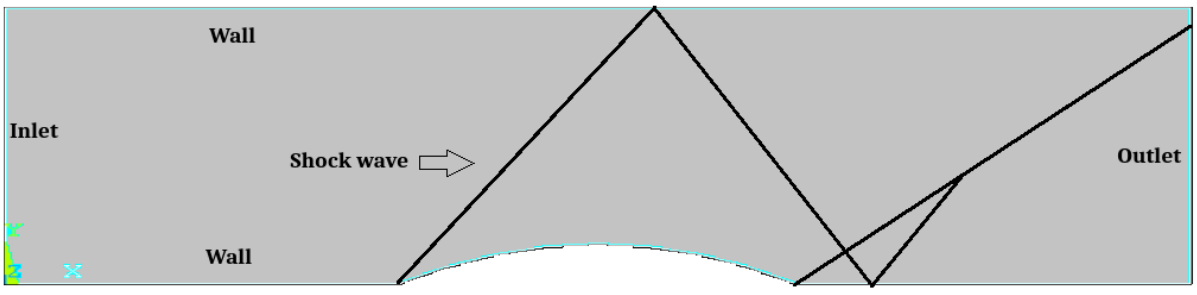

Source: The author.

Figures 9, 10 and 11 show the contours for the Mach number, pressure and density, respectively.

Figure 9

Mach

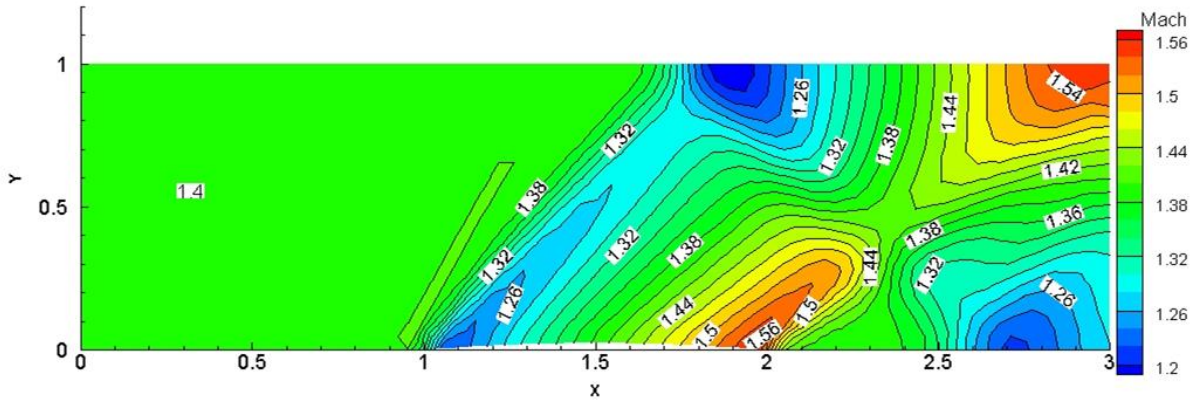

Source: The author.

The expected effect with respect to the formation of shock waves can be seen in Fig. 8. In Figure 9, the formation of two shock waves and their junction can be observed, as well as the decrease in the Mach number immediately after the formation of the shock.

Figure 10

Pressure contours [Pa]

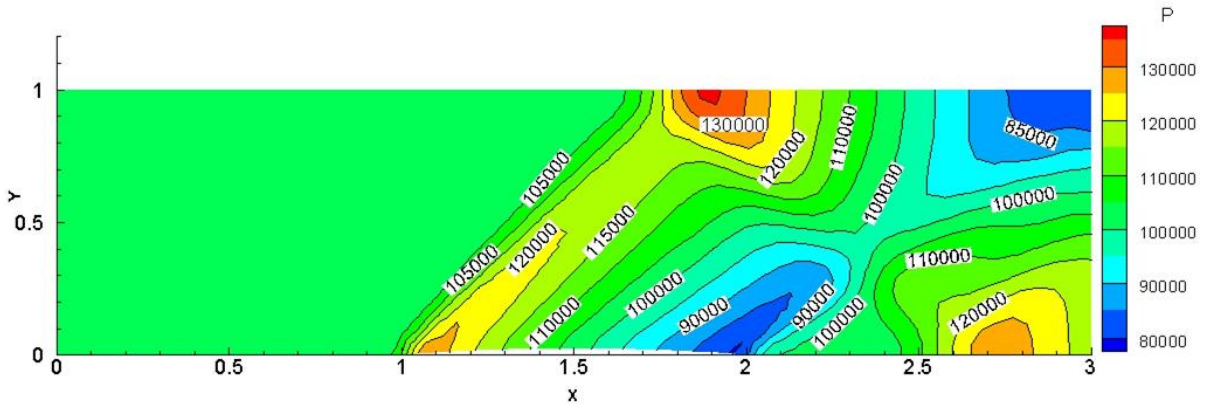

Source: The author.

Figure 11

Density contours [kg/m3]

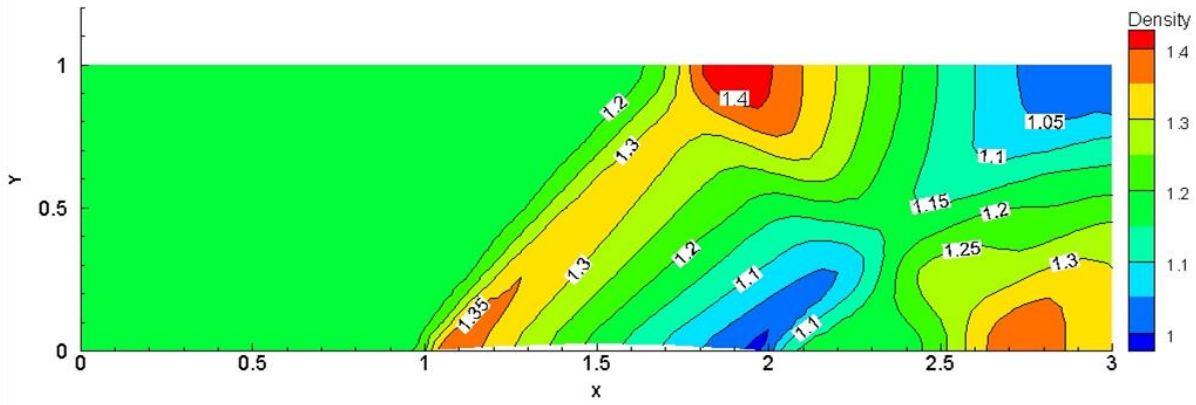

Source: The author.

For the cases of pressure and density isovalues, Figs. 10 and 11, respectively, it is observed the representation of a decrease in the values of pressure and density after the region where the shock wave occurs, which reproduces the expected physical characteristics.

Fig. 12 shows the values for the Mach number along the bottom wall of the channel. To verify the numerical precision of the results obtained in this simulation, the results were compared with values obtained in the literature, (AKDEMIR, 2010).

Figure 12

Mach number on the wall at the bottom wall of the channel.

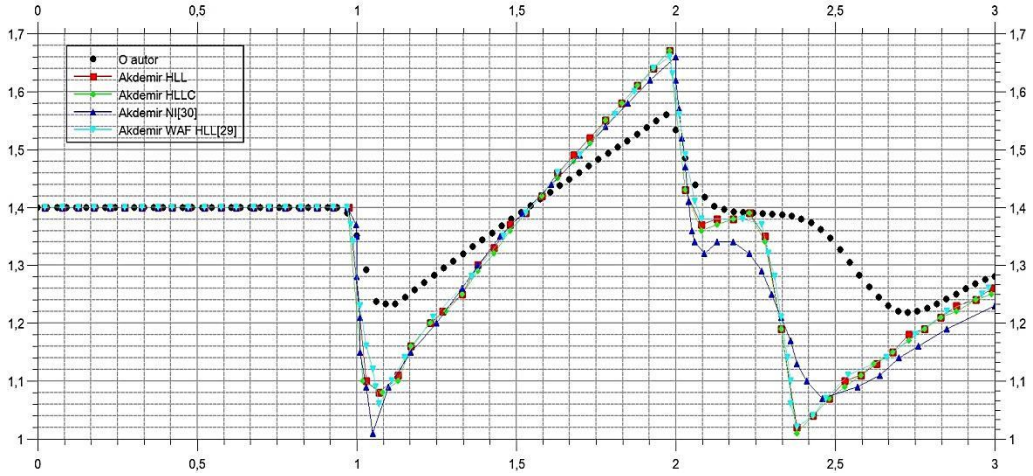

Source: The author.

Fig. 13 shows the values for the Mach number along the upper wall of the channel. Again, the results of this simulation were compared with results from the literature, (AKDEMIR, 2010), to verify the numerical precision of the results obtained here.

Figure 13

Mach number on the upper wall of the channel.

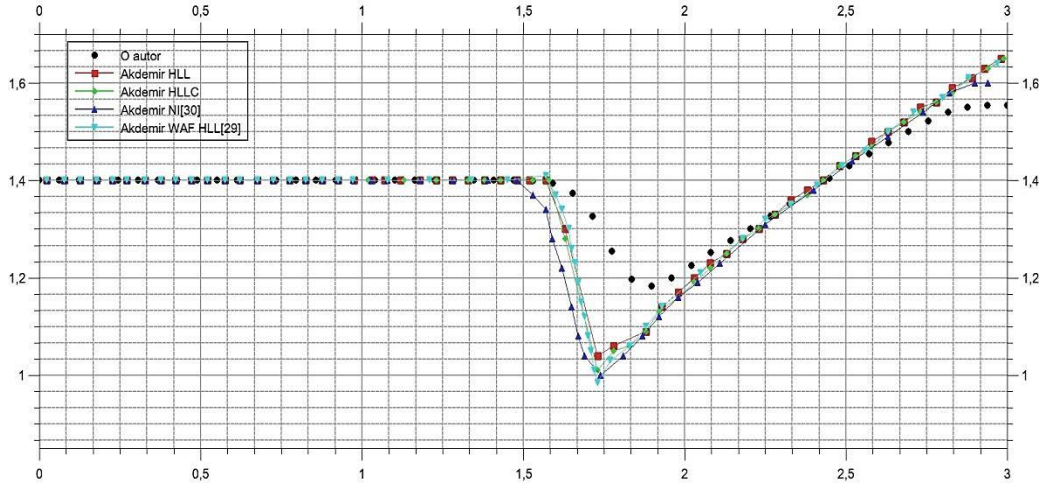

Source: The author.

The results obtained in the present work for the Mach number, Figures 12 and 13, present a behavior similar to the results in the literature, being slightly distant because the mesh used is not thin enough to bring more precision to the results.

4.1.2 Prandtl–Meyer expansion

For this case, the main reference was Ollivier-Gooch (2003). The geometry and its dimensions can be seen in Fig. 14. The boundary conditions for this simulation are presented in detail in Ollivier-Gooch (2003). The mesh used, represented in Figure 14, has 2488 control volumes and 1337 nodes.

Figure 14

Mesh for the Prandtl-Meyer expansion case

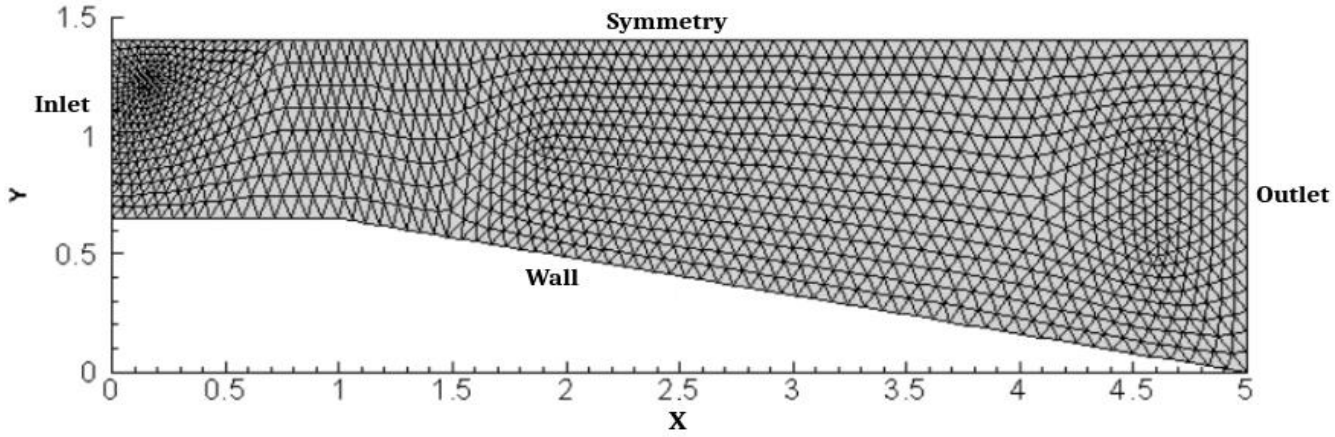

Source: The author.

To perform this simulation, the following initial condition is assumed

$$\frac{P}{P_o} = 7{,}8244 \qquad (22)$$

$$\frac{T}{T_o} = 1{,}8 \qquad (23)$$

With these relations we have the Mach number of the flow equal to 2, Ollivier-Gooch (2003).

The expected behavior for the flow is represented in Fig. 15. Due to the variation in geometry, it is expected to observe the opening of expansion fans, which make the fluid adapt to the new flow direction gradually. The flow should also gain speed to the exit region, implying an increase in the number of Mach and a decrease in pressure and density values after passing through the expansion fan.

Figure 15

Expected result for Prandtl-Meyer Expansion

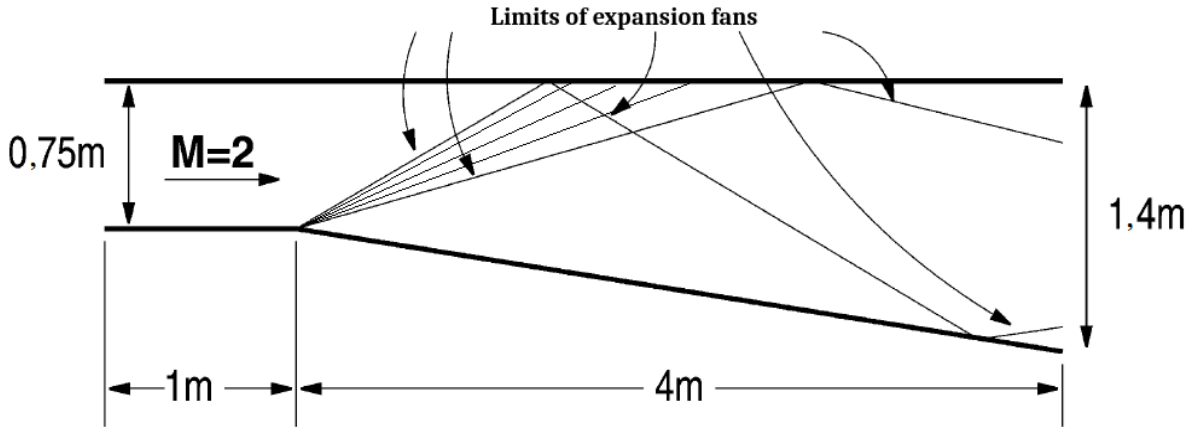

Source: Modified – Ollivier-Gooch, Carl (2003).

Figures 16, 17 and 18 show the isovalues of Mach number, pressure and density, respectively for the simulated case using Euler's equations.

Figure 16

Representation of the Mach number

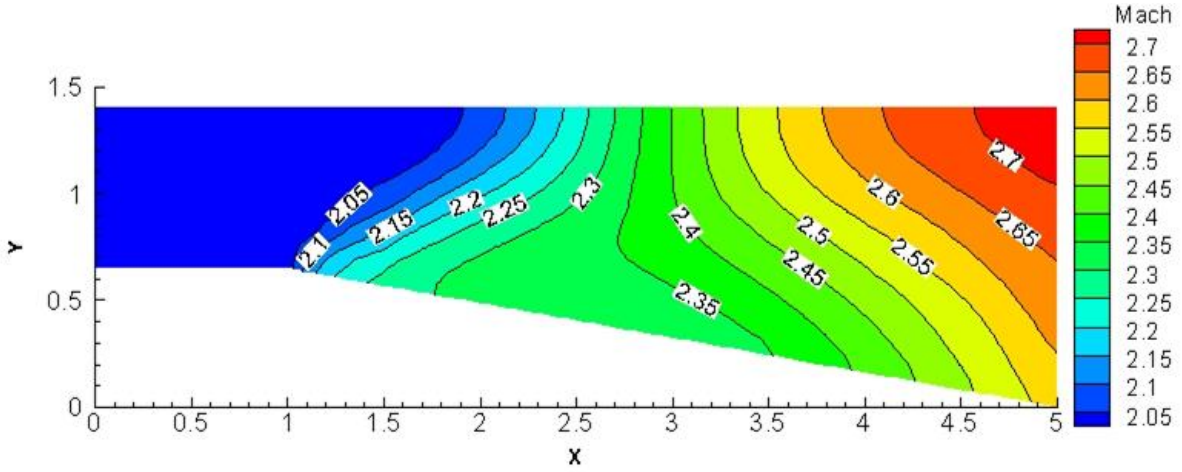

Source: The author.

The Mach number isovalues in Figure 16 depict the formation of the expansion fan at position x = 1 and the Mach number increasing up to the output region.

Figure 17

Representation of pressure [Pa]

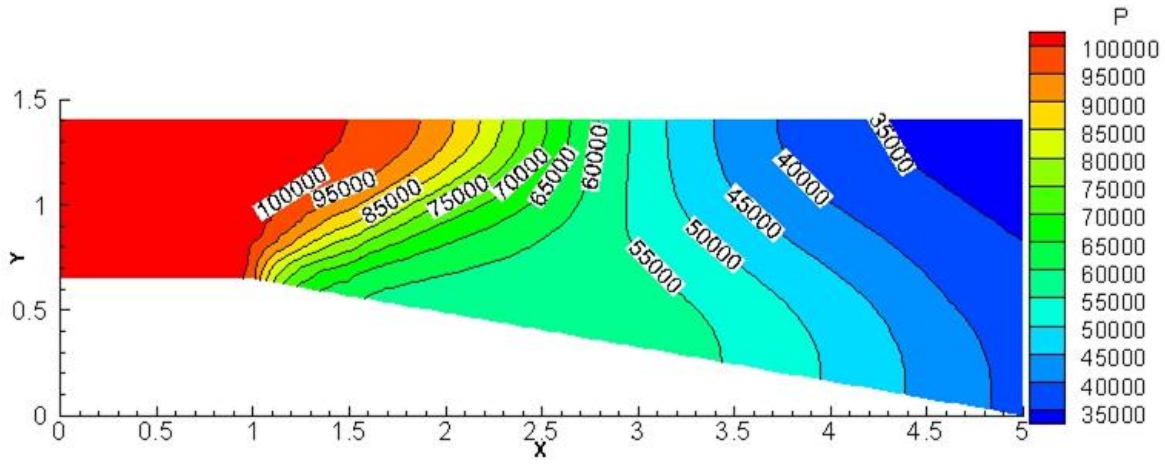

Source: The author.

Figure 18

Representation of density [kg/m3].

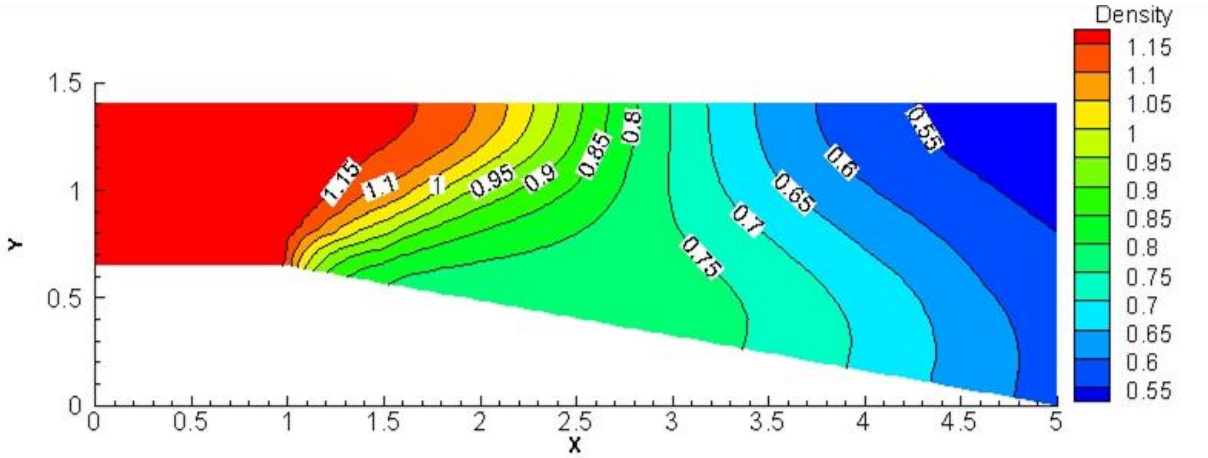

Source: The author.

Figures 17 and 18 depict the decrease in pressure and density after passing through the expansion range, an expected result that corroborates the achievement of results faithful to the physics of the problem.

The results for the Mach number found by Ollivier-Gooch (2003) can be compared with the results obtained in the present study. This comparison can be seen in Fig. 19, where it is possible to notice the similar behavior for the Mach number ("y" axis) verified along the symmetry axis ("x" axis). One factor that could have made the results of this work closer to those of Ollivier-Gooch (2003) is the mesh used, which could be more refined. However, the physical behavior of the problem was similar, which shows that the ***HYNE2D code*** reproduces the results with physical coherence.

Figure 19

Comparison of the Mach number on the symmetry axis.

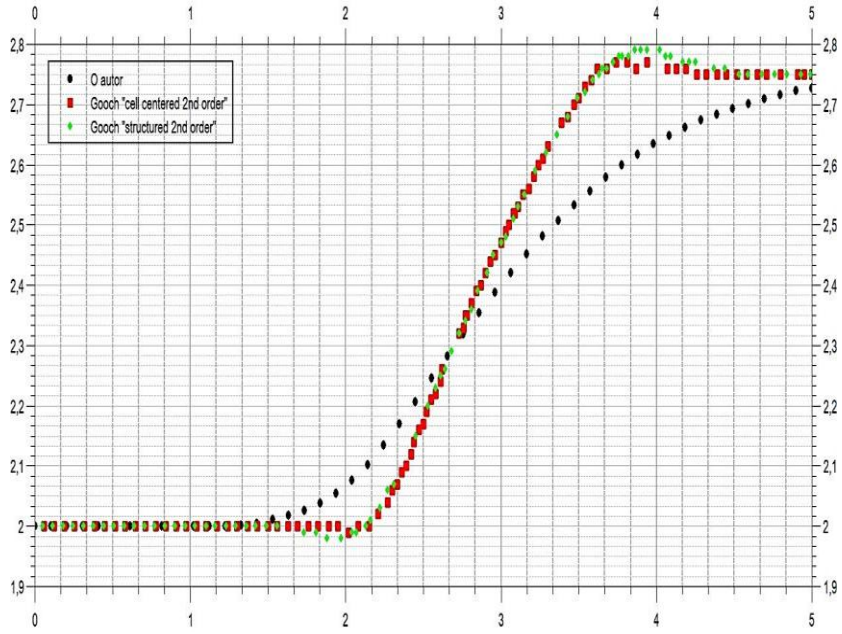

Source: The author.

4.1.3 Bell Type Nozzle

This case is based on the work of Cruz-Salvador (2005). The geometry, according to Cruz-Salvador (2005), is indicated in Fig. 20. The input, output, wall, and symmetry regions are indicated in Fig. 21, along with the mesh of 2336 control volumes and 1289 nodes.

To perform this simulation, the following initial condition is assumed

$$P_o = 861262{,}5[Pa]$$
$$T_o = 417{,}3[K]$$
$$P_{saída} = 101325[Pa] \qquad (24)$$

With these relationships we have the Mach number of the flow equal to 3, Cruz-Salvador (2005).

Figure 20

Geometry for bell nozzle

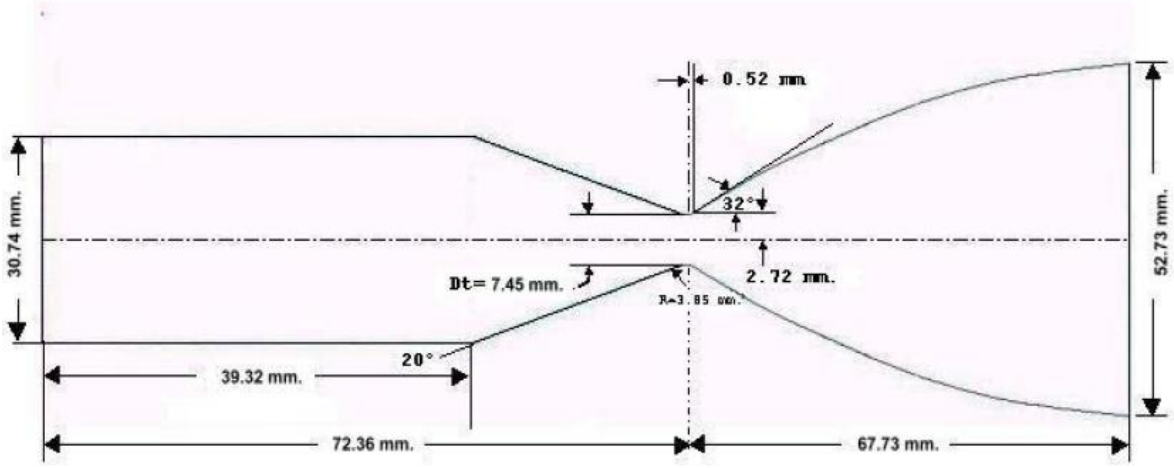

Source: Cruz-alvador, Nícolas M. (2005).

Figure 21

Mesh for the case

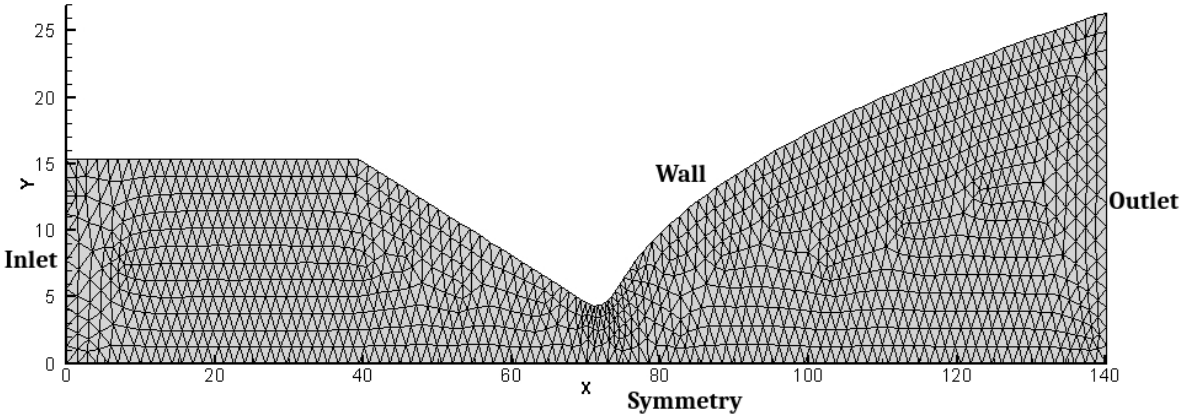

Source: The author.

For this case it is intended to show the evolution of the Mach number, pressure and density over time until the end of the numerical simulation, determined by the halting criterion. This representation is indicated in Figures 22, 24 and 26, respectively. The order of the figures with their relation in time is indicated by the alphabetical identification.

The interest in this geometry is special because it is probably the most common geometry among modern rockets (SUTTON; BIBLARZ, 2000). NASA's reusable orbiter, as an example, uses RS-25 engines based on Laval's geometry (NASA, 2009).

Figure 22

Evolution of the Mach number in relation to time

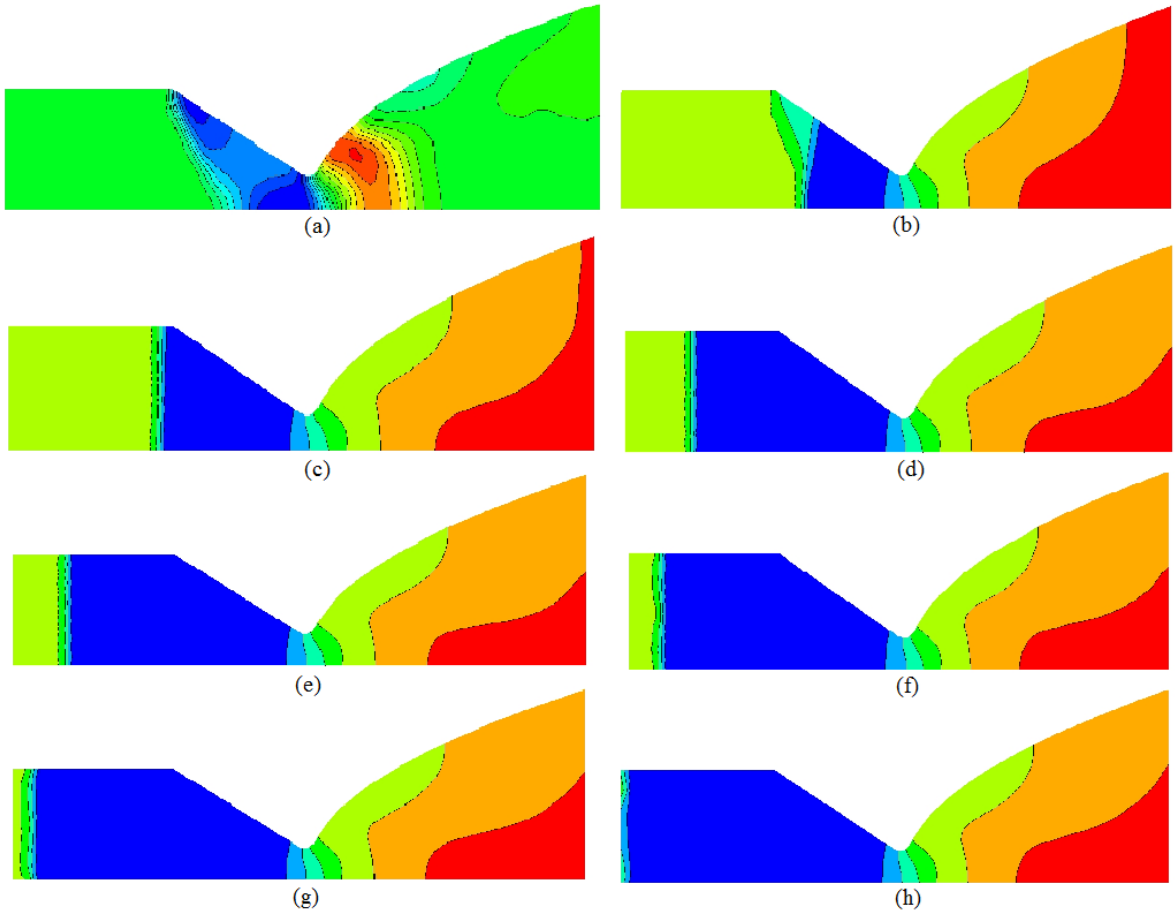

Source: The author.

Figure 23

Representation of the Mach number

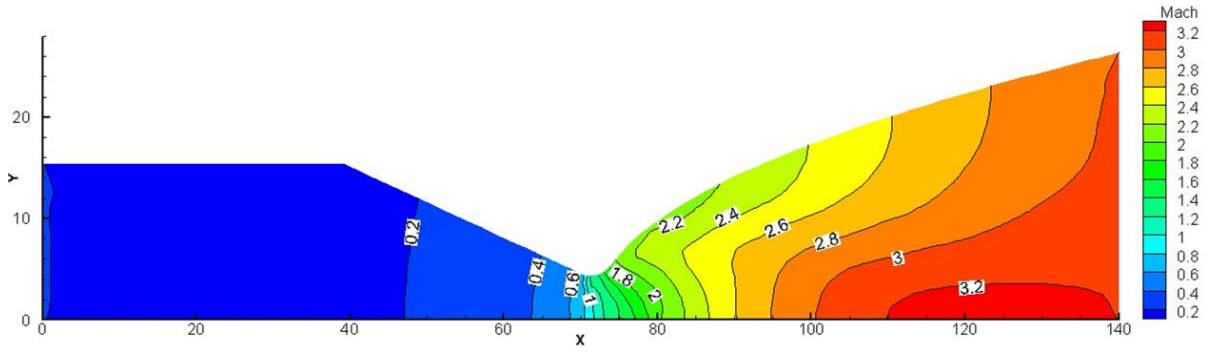

Source: The author.

Fig. 22 represents the behavior of the Mach number at eight different instants, where the chronological order is given through the alphabetical order of the items in the figure. It is possible to notice the evolution of the flow along the nozzle in the direction of departure. While in the opposite direction, a reflected shock wave shifts the flow from the direction of the rocket

engine's intake. It is observed that the first region to be stabilized is the throat, where the Mach number must be equal to 1. From this point on, the values are gradually stabilized both in the direction of the inlet and outlet of the gases. The representation in Fig. 23 is the situation of the Mach number at the final instant where it is possible to confirm the Mach number equal to 1 in the throat and the acceleration of the fluid to the outlet section.

Figure 24

Evolution of pressure [Pa] in relation to time

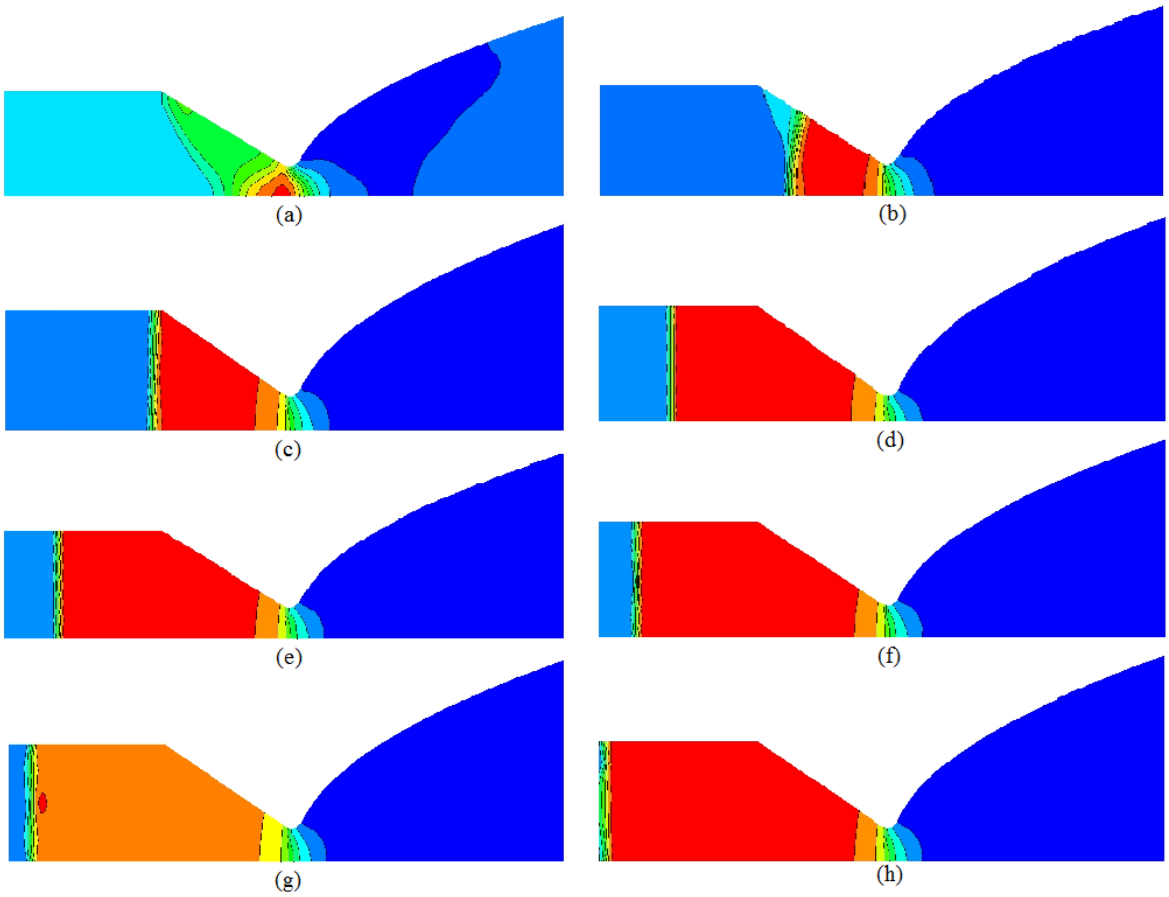

Source: The author.

Figure 25

Representation of pressure [Pa]

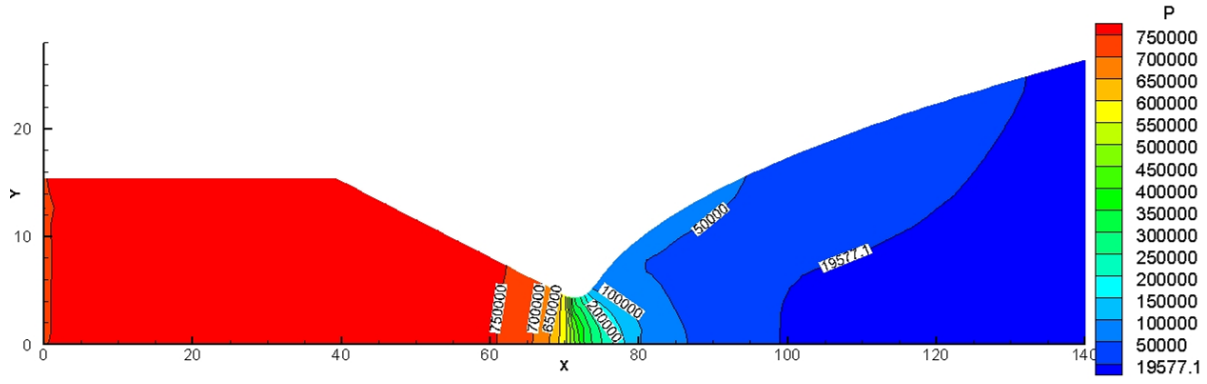

Source: The author.

The representation of the pressure isovalue curves over time portrays that the last zone to be stabilized is the region that represents the rocket's combustion chamber. This region has the highest pressure values precisely because it is the combustion zone. Soon after the flow passes through the throat, the gas expands and the pressure has considerably lower values. It is noted that the drop in pressure is rapid, as indicated in the literature and in this study shown in Fig. 24.

At the final instant of the simulation, the pressure distribution along the rocket engine can be verified by the pressure isovalues shown in Fig. 25. In the pressure isovalues, a sharp drop in the pressure of the throat region and relatively low values in the exit section are observed, in contrast to the values where the combustion of gases occurs, in this representation on the left side of the throat.

Figure 26

Evolution of density [kg/m3] over time

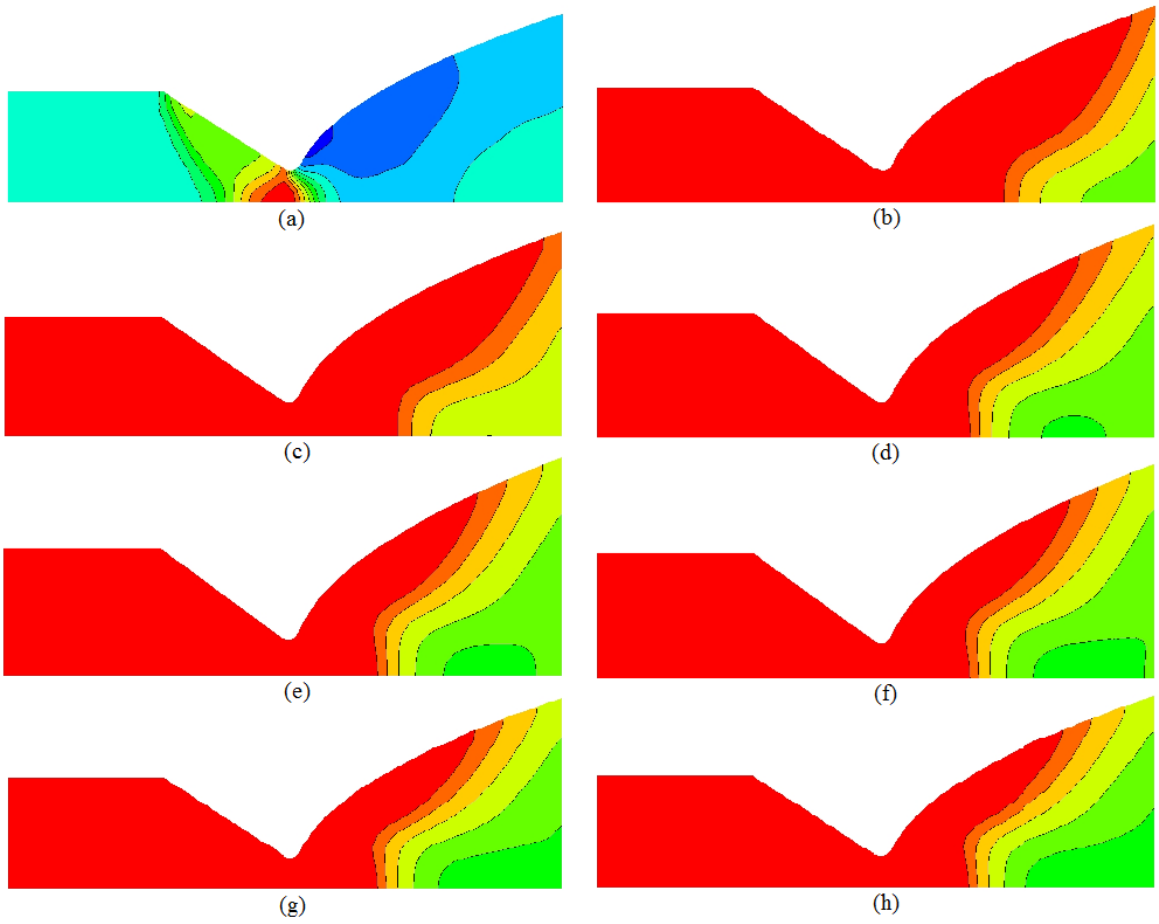

Source: The author.

Figure 27

Representation of density [kg/m3]

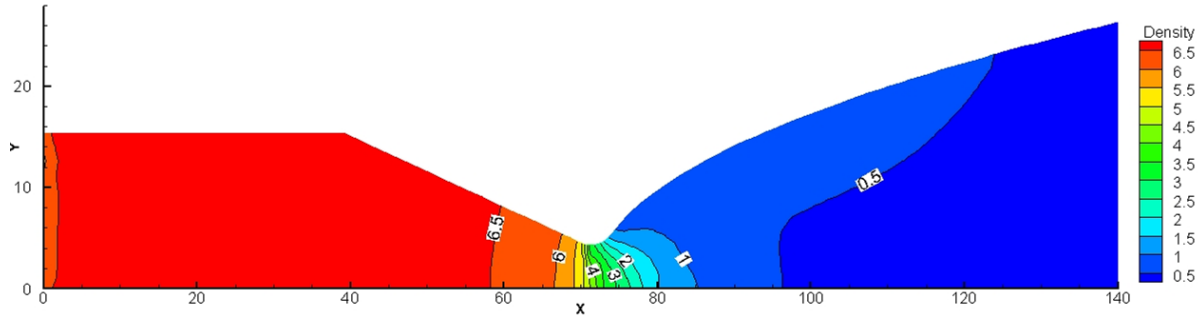

Source: The author.

The evolution of the density shows that this property is gradually decreasing in the direction of the output section, Fig. 26. In the exit section of the rocket engine, a divergent region, the density decreases sharply because the thermal energy and pressure are converted into kinetic energy, causing the expansion of the gas, which promotes its acceleration in the direction of the nozzle exit. In the expansion process, the net volume to accommodate the gas molecules increases, providing greater scattering of the molecules, decreasing the density of the gas. Which can be observed in the density isovalues at the final instant of the simulation, Fig. 27.

4.1.4 Conical Nozzle

For the study of this case, the work of Akdemir (2010) is again used as a reference. The geometry and regions considered as input, output, wall and symmetry are indicated in Fig. 28. The wall in the region representing the combustion chamber is 170 mm long and the transition radius of curvature between the combustion chamber and the throat of the nozzle is 45 mm. The radius of the throat region of the mouthpiece has the dimension of 16.7 mm and the total length is 270 mm.

The mesh for this case has 2300 control volumes and 1254 nodes, Fig. 28. The initial condition for performing the numerical simulation is given by

$$P_o = 861262{,}5[Pa]$$
$$T_o = 417{,}3[K]$$
$$P_{saída} = 101325[Pa] \qquad (25)$$

With these relationships we have the number of Mach equal to 3, Akdemir (2010).

Figure 28

Mesh representation

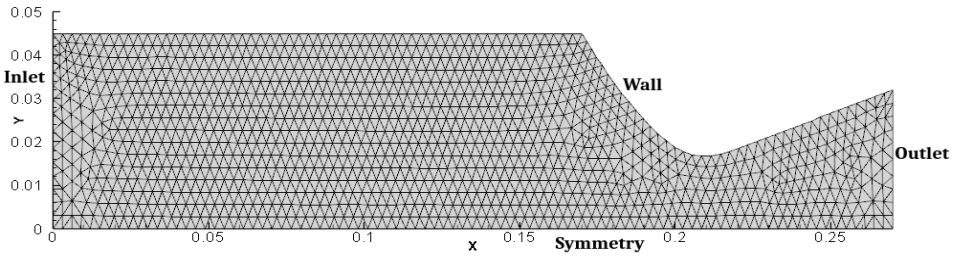

Source: The author.

In figures 29, 30 and 31 we have the isovalues for the representation of the Mach number, pressure and density, respectively.

Figure 29

Representation of the Mach number

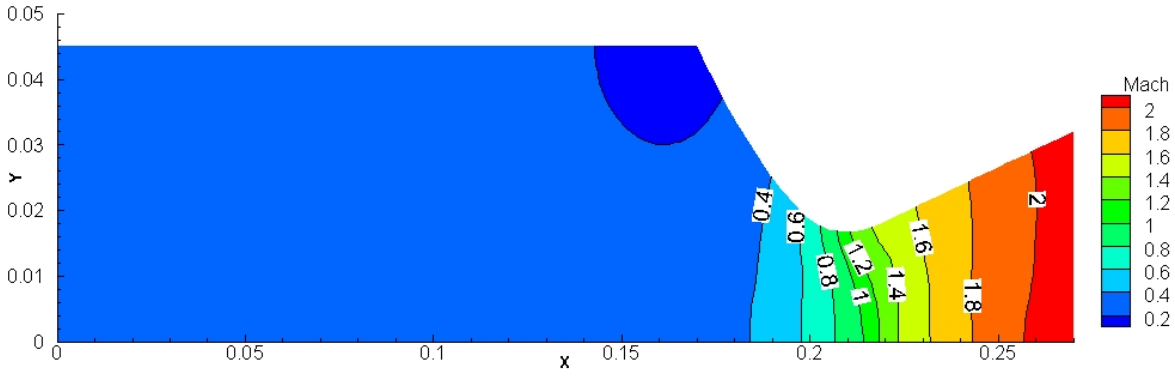

Source: The author.

It is observed in Fig. 29 that the code ***HYNE2D*** Mach number equal to 1 in the throat with subsequent acceleration of the gases in the direction of the nozzle exit.

The interpretation of the results obtained for pressure and density in this simulation, figures 30 and 31, are very similar to those described in the case of item 4.1.3. It is only worth mentioning that in this case the mouthpiece has a conical shape.

Figure 30

Representation of the pressure [Pa]

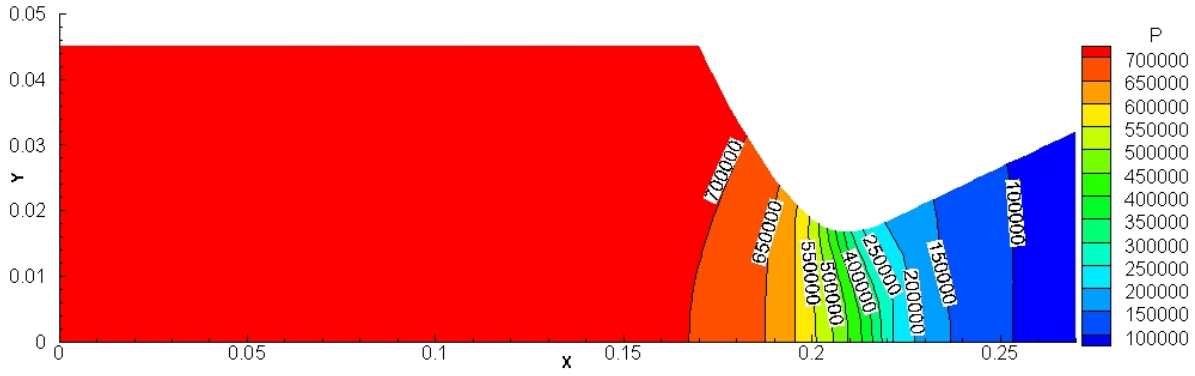

Source: The author.

Figure 31

Representation of density [kg/m3]

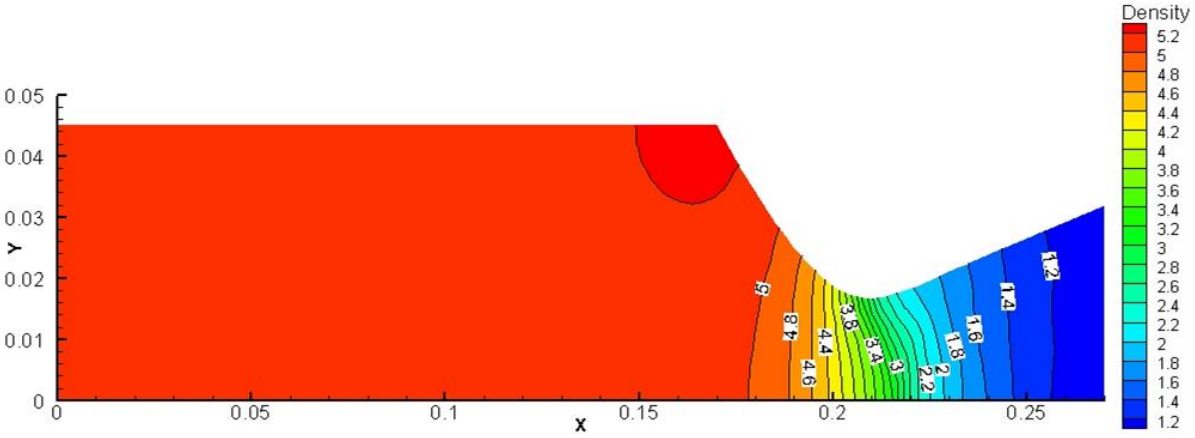

Source: The author.

hrough comparisons with the literature, cases 4.1.1 and 4.1.2, it is observed that the ***HYNE2D*** code reproduced results with physical coherence for the simulations involving Euler's equations. Differing in the accuracy of the results when compared with the results in the literature, due to the use of thicker meshes. Results with greater precision can be obtained by the use of thinner meshes, i.e., with a greater number of control volumes.

It is important to remember that the high-resolution method used in the present simulations reproduced a Mach number equal to 1 in the throat of rocket engines with bell and conical nozzles, figures 23 and 29, respectively. The numerical stability provided by the Roe method in the simulations of Euler's equations was crucial to obtain the Mach number equal to 1 in the throat. The present entropy corrections implemented in the method preserves numerical stability during the compression and exposure process of the gas

passing through the throat. Enabling the achievement of high-resolution results for shock waves and expansion along geometries.

To verify the effectiveness of the high-resolution method implemented in the ***HYNE2D*** code, numerical simulations of compressible fluid flow were performed for the Navier-Stokes equations, i.e., with the presence of viscosity. The results are presented and analyzed from item 4.2.

4.2 VISCOUS FLOW

To consider the effect of viscosity, the Navier-Stokes equations are used to represent the behavior of the flow properties. For these cases we can analyze the behavior of the temperature in the flow. The use of these equations implies greater computational demand.

The three case studies in this topic are the same as those simulated with Euler's equations. Therefore, the simulations were performed in the same geometries and meshes, whose considerations of the input, output, wall and symmetry regions are the same, figures 14, 21 and 28.

The main objective of these simulations is to verify if the high-resolution method reproduces the shock and expansion waves with physical coherence throughout the geometries. In particular, the number of Mach equal to 1 in the throat in the simulations of the nozzles with bell and conical nozzles. Therefore, the same boundary condition was used for the three simulations

$$P_o = 861262{,}5[Pa]$$
$$T_o = 3387[K]$$
$$P_{saída} = 101325[Pa] \qquad (26)$$

With these relations, we have the Mach number of the flow equal to 3.

4.2.1 Prandtl–Meyer expansion

Figures 32, 33, 34, and 35 are representations of the isovalues for the Mach number, pressure, density, and temperature, respectively.

Figure 32

Representation of the Mach number (Navier-Stokes)

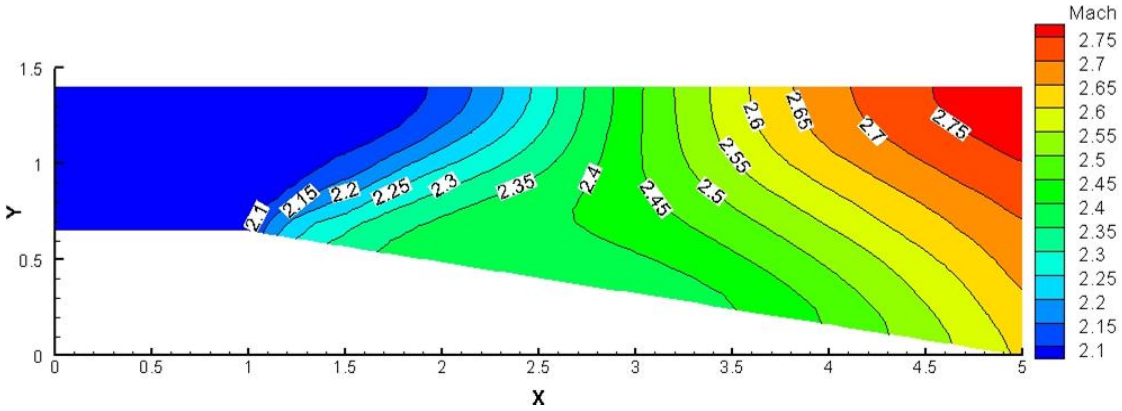

Source: The author.

The interpretation of Fig. 32 is similar to the case of the same geometry for the non-viscous case, Fig. 16. The expansion fan opens at the x-position equals one, and the velocity increases until the geometry exits. For this case, slightly higher values for the Mach number are observed because the initial condition for this case is different from the one used in the simulation of the non-viscous case.

Figure 33

Representation of pressure [Pa] (Navier-Stokes)

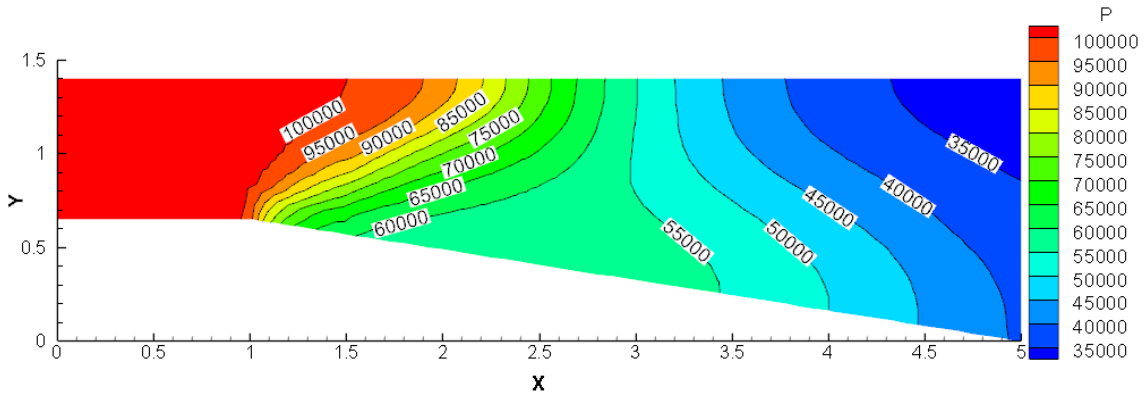

Source: The author.

Figure 34

Representation of density [kg/m3] (Navier-Stokes)

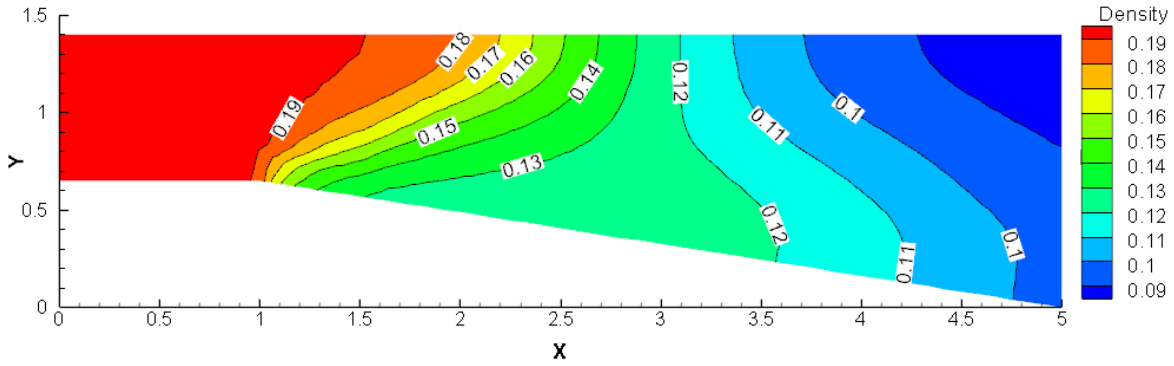

Source: The author.

Figure 35

Representation of temperature [K] (Navier-Stokes)

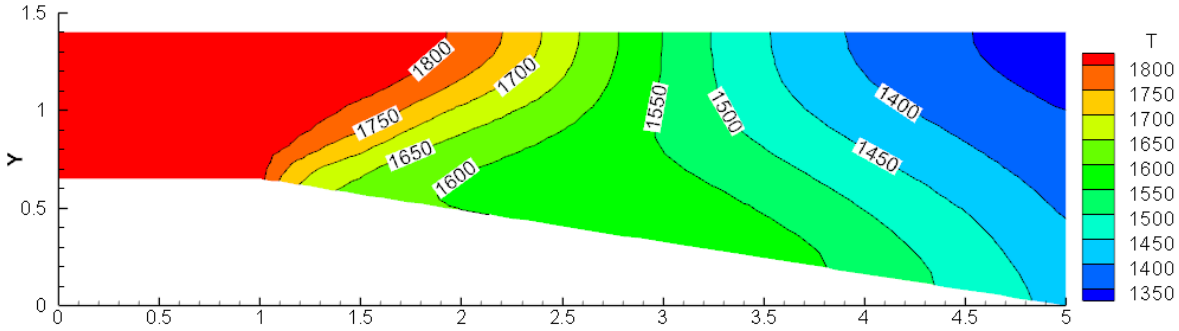

Source: The author.

Figures 33, 34 and 35 represent the behavior of pressure, density and temperature respectively. For these cases, it is noted that the values of these properties fall after the gas passes through the divergent region of the geometry, where the expansion range is formed at the x-position equal to one, Fig. 32, inverse behavior to the Mach number. With the expansion of the gas in the divergent region, the pressure and density decrease, as well as the thermal energy, due to the conversion into kinetic energy.

4.2.2 Bell Type Nozzle

Figures 36, 37, 38, and 39 are representations of the isovalues of Mach number, pressure, density, and temperature, respectively.

Figure 36

Representation of the Mach number (Navier-Stokes)

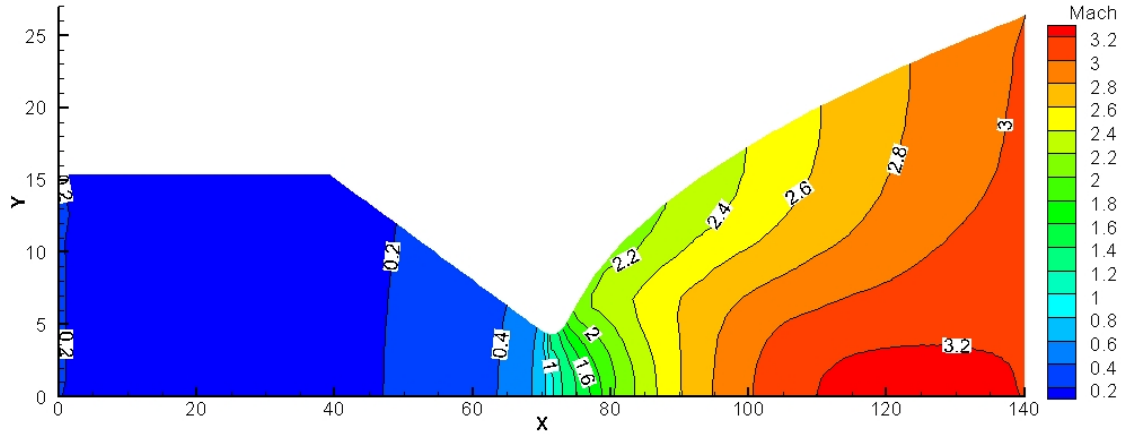

Source: The author.

Figure 37

Representation of pressure [Pa] (Navier-Stokes)

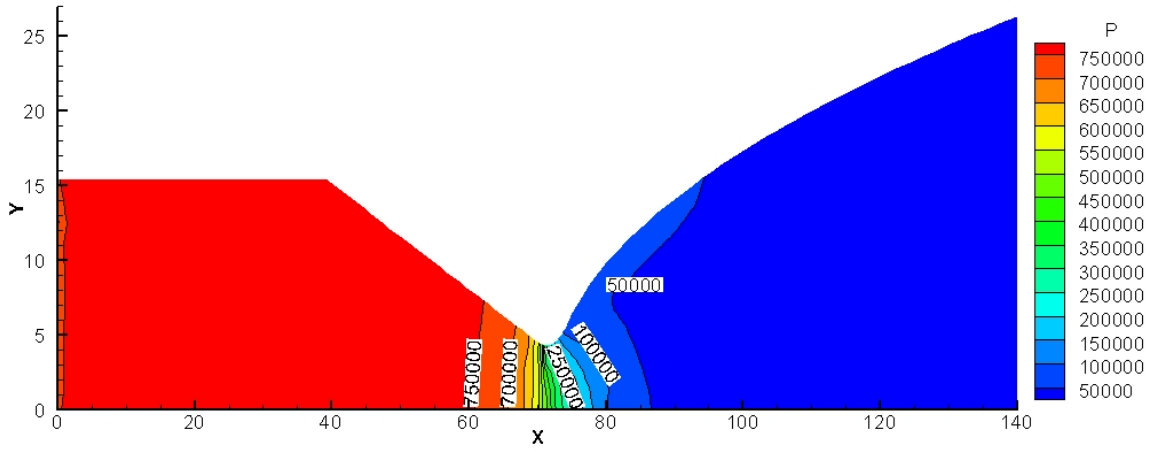

Source: The author.

Figure 38

Representation of density [kg/m3] (Navier-Stokes)

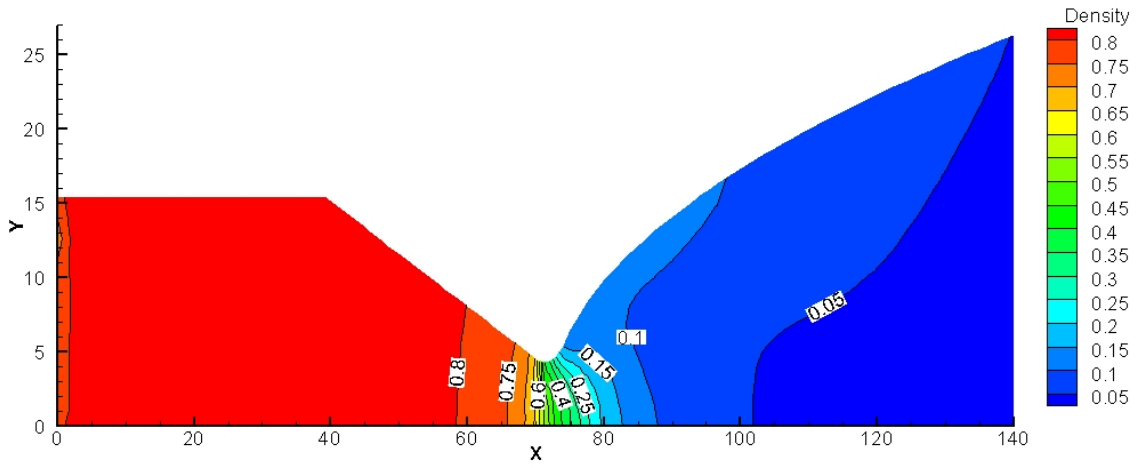

Source: The author.

Figure 39

Representation of temperature [K] (Navier-Stokes)

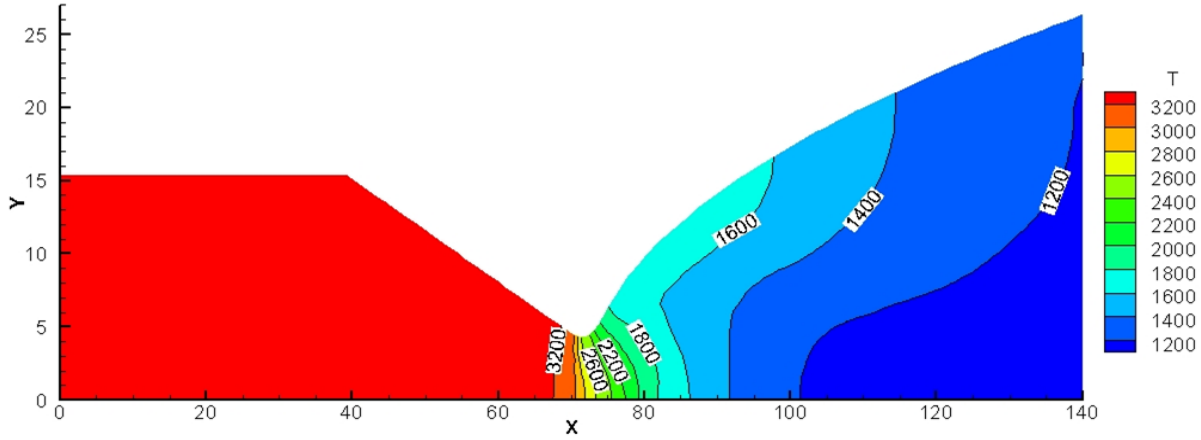

Source: The author.

Observing the values of the properties for the viscous flow along the bell-type pipe, it is observed that the ***HYNE2D code*** reproduced the flow behavior as seen in the literature. The highlight is the throat region, where the Mach number is equal to one, Fig. 36. You can also observe that before this point we have subsonic velocities, with a Mach number less than one, while pressure, density and temperature have their highest values. After the gas passes through the throat, there is an expansion of the gas, which causes a sharp drop in pressure, density and temperature. In the divergent region there is the conversion into kinetic energy, which causes the increase in the number of Mach and in the output region we observe the speed about three times greater than the speed of sound.

The values of the pressure, density and temperature properties, figures 37, 38 and 39, decrease as a consequence of the expansion of the gas through the divergent region of the nozzle. Effect of converting thermal energy into kinetic energy, increasing the number of Mach at the nozzle output.

4.2.3 Conical Tubing

Figures 40, 41, 42, and 43 are representations of the isovalues of Mach number, pressure, density, and temperature, respectively.

Figure 40

Representation of the Mach number (Navier-Stokes)

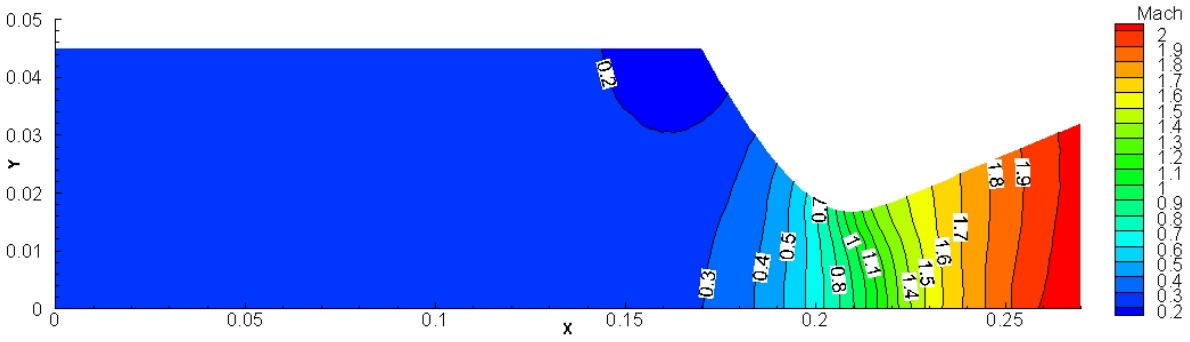

Source: The author.

Figure 41

Representation of pressure [Pa] (Navier-Stokes)

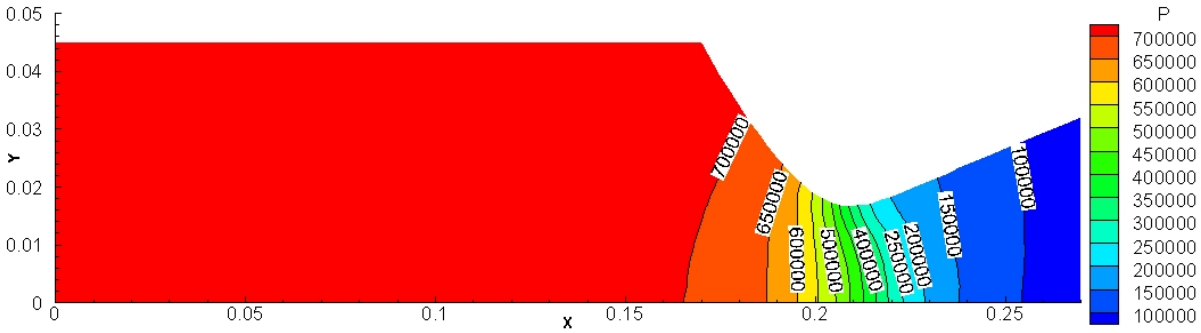

Source: The author.

Figure 42

Representation of density [kg/m3] (Navier-Stokes)

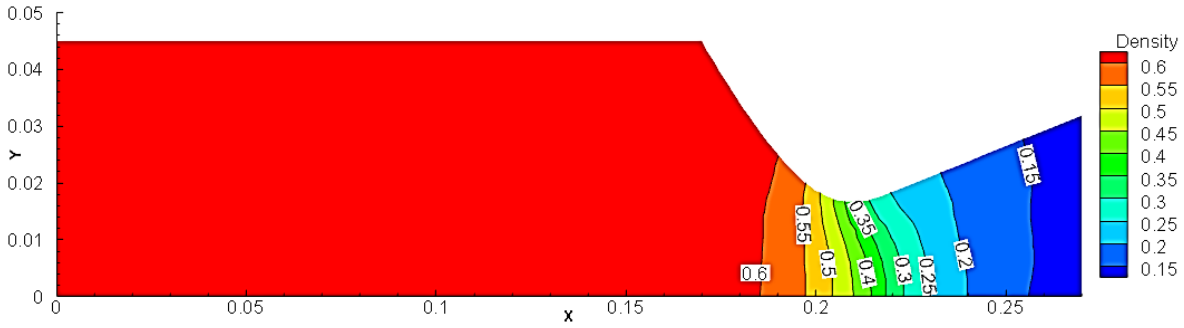

Source: The author.

Figure 43

Representation of temperature [K] (Navier-Stokes)

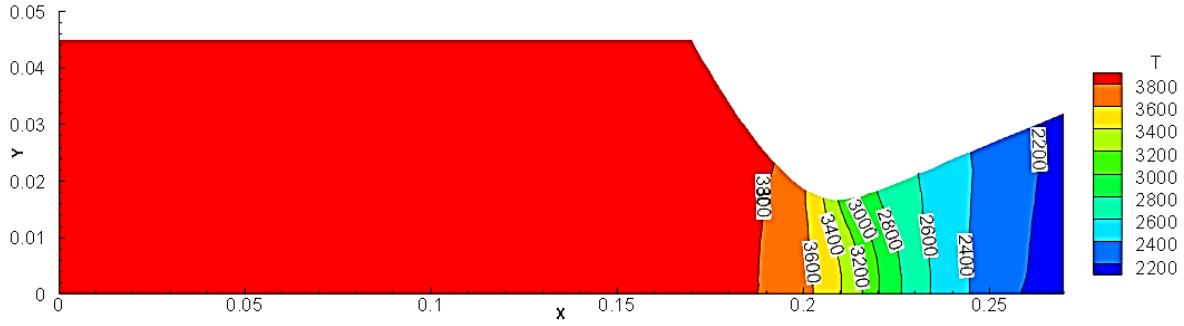

Source: The author.

Because we have the same initial condition as in the case of the bell-type nozzle, the analysis of the isovalues of Mach number, pressure, density and temperature are quite similar. With the expansion of the gas in the divergent region, the pressure, density and temperature decrease, reducing the thermal energy. This physical effect causes the conversion into kinetic energy, increasing the number of Mach at the exit of the nozzle.

4.2.4 Mach number at throat of bell and conical tubers

The isovalues of the Mach number for the bell and conical type tubers are represented here, figures 44 and 45, respectively, with emphasis on the throat region.

Figure 44

Mach number in the throat of the bell tube

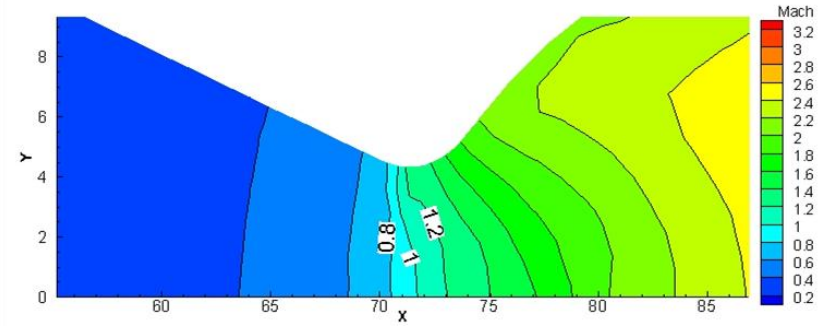

Source: The author.

Figure 45

Mach number in the throat of the conical nozzle

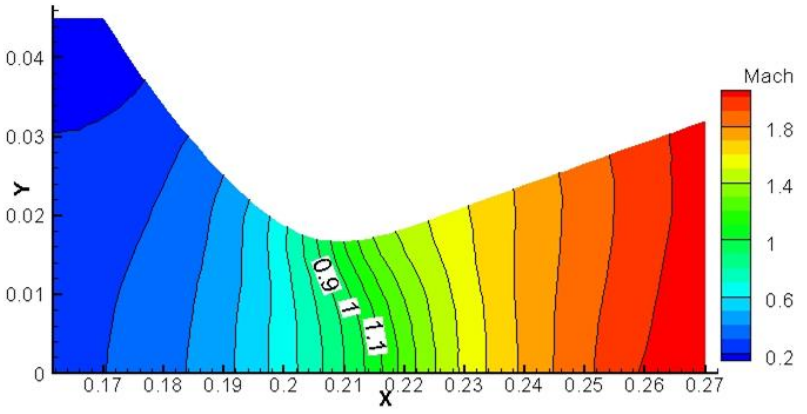

Source: The author.

In these results, the behavior of the Mach number in the throat region can be seen, which, according to the literature, must be equal to one. In both simulations, the code ***HYNE2D*** reproduced the flow with a male number equal to one in the throat.

With the physical coherence obtained in these results, it was possible to verify that the high-resolution schemes together with the Roe method maintained numerical stability in the simulations of viscous flow in unstructured meshes. The numerical scheme used to calculate the viscous flow also maintained numerical stability and did not cause loss of precision in the calculation of the derivatives.

5 CONCLUSION

In the present work, supersonic flows of compressible fluid in the nozzles, geometry used in rocket engines, were numerically simulated. To analyze the flow pattern through nozzles, the Euler equations and the Navier-Stokes equations, i.e., echoes without viscosity effect and with viscosity effect, respectively, were simulated.

In the simulations for Euler's equations, the physical coherence of the results was verified, which were compared with the correlated literature. In the simulations for the Navier-Stokes equations, the behavior of temperature and consequently the conversion of thermal energy into kinetic energy was verified. The ***HYNE2D*** code showed numerical stability in all the simulated cases in this work. Due to the high computational cost of these simulations, thicker meshes were used in the numerical simulations. Even though the simulations were performed in thick meshes, the results obtained with the ***HYNE2D*** code maintained good accuracy when compared to the related literature.

In the simulations considering the Navier-Stokes equations, the initial condition for all cases was the same. The Mach number at the end of the divergent region in the bell nozzle is greater than in the conical nozzle. Indicating that the bell-type nozzle is more efficient than the conical nozzle, as it accelerates the gas in the divergent region with greater intensity. Therefore, it is more suitable for aerospace applications such as rocket engines.

To improve the accuracy of the results, it is necessary to simulate in thinner meshes than those used in the present work. However, it is necessary to consider the real need for refinement, as the computational cost increases exponentially with the refinement of the mesh, mainly to simulate models with viscous effect flow. In the Navier-Stokes equations, the computational cost is higher, because the derivatives of the term viscous are added to the calculations, lacking a specific numerical scheme that involves the geometric characteristics to obtain the values of the derivatives. That considerably increases the computational cost of simulations being outside the scope of the present work, and is therefore the result of future investigations.

REFERENCES

Ahrens, J., Geveci, B., & Law, C. (2005). ParaView: An end-user tool for large data visualization. In C. D. Hansen & C. R. Johnson (Eds.), The visualization handbook (pp. 717–731). Elsevier.

Akdemir, M. (2010). Development of an axisymmetric, turbulent and unstructured Navier-Stokes solver [Master's thesis, Middle East Technical University].

Anderson, J. D. (2003). Modern compressible flow, with historical perspective (3rd ed.). McGraw-Hill.

Barros, J. E. M. (n.d.). Propulsão II: Motores foguete bocais convergente-divergente. Mautone Engenharia. http://www.mautone.eng.br

Blazek, J. (2005). Computational fluid dynamics: Principles and applications (2nd ed.). Elsevier. (Original work published 2001)

Cengel, Y. A., & Boles, M. A. (2015). Thermodynamics: An engineering approach (8th ed.). McGraw-Hill Education. (Original work published 2006)

Cruz-Salvador, N. M. (2005). Simulação numérica do escoamento em um motor foguete com reação química [Master's thesis, Instituto Nacional de Pesquisas Espaciais]. INPE.

Fox, R. W., McDonald, A. T., & Pritchard, P. J. (2009). Introdução à mecânica dos fluidos (7ª ed.). LTC. (Original work published 2004)

Geuzaine, C., & Remacle, J.-F. (2009). Gmsh: A three-dimensional finite element mesh generator with built-in pre- and post-processing facilities. International Journal for Numerical Methods in Engineering, 79(11), 1309–1331. https://doi.org/10.1002/nme.2579

GNU Project. (n.d.). The GNU Fortran compiler. GCC Online Documentation. Retrieved December 10, 2025, from https://gcc.gnu.org/onlinedocs/gfortran/

Gomes, F. A. A. (2012). Análise numérica do escoamento hipersônico em torno de corpos rombudos utilizando métodos de alta ordem [Doctoral dissertation, Instituto Tecnológico de Aeronáutica]. ITA.

Gottlieb, S., & Shu, C.-W. (1998). Total variation diminishing Runge-Kutta schemes. Mathematics of Computation, 67(221), 73–85. https://doi.org/10.1090/S0025-5718-98-00913-2

Hirsch, C. (2007). Numerical computation of internal and external flows: Fundamentals of computational fluid dynamics (Vol. 1, 2nd ed.). Elsevier.

Hirsch, C. (1990). Numerical computation of internal and external flows: Computational methods for inviscid and viscous flows (Vol. 2). Wiley. (Original work published 1988)

Hoffman, J. D. (1987). Design of compressed truncated perfect nozzles. Journal of Propulsion and Power, 3(2), 150–156. https://doi.org/10.2514/3.22972

Jawahar, P., & Kamath, H. (2000). A high-resolution procedure for Euler and Navier-Stokes computations on unstructured grids. Journal of Computational Physics, 164(1), 165–203. https://doi.org/10.1006/jcph.2000.6584

Kitamura, K., & Shima, E. (2012). Simple and parameter-free second slope limiter for unstructured grid aerodynamic simulation. AIAA Journal, 50(6), 1415–1426. https://doi.org/10.2514/1.J051459

Laroca, F. (2000). Solução de escoamentos reativos em bocais de expansão usando o método dos volumes finitos [Master's thesis, Universidade Federal de Santa Catarina]. UFSC.

LeVeque, R. J. (2002). Finite volume methods for hyperbolic problems. Cambridge University Press.

Lorena, D. (2014). El sector espacial argentino: Instituciones referentes, proveedores y desafíos. ARSAT – Empresa Argentina de Soluciones Satelitales.

Makris, K. (n.d.). Nozzle design. Retrieved November 10, 2025, from https://www.k-makris.gr/nozzle-design/

Miraglia, J. (1995). Propulsão. [Publisher not identified].

Mourão, R. R. F. (1999). Astronáutica: Do sonho à realidade. Bertrand Brasil.

National Aeronautics and Space Administration. (2009). Space Shuttle main engines. NASA. https://www.nasa.gov/returntoflight/system/system_SSME.html

Nishikawa, H., & Kitamura, K. (2008). Very simple, carbuncle-free, boundary-layer-resolving, rotated-hybrid Riemann solvers. Journal of Computational Physics, 227(4), 2560–2581. https://doi.org/10.1016/j.jcp.2007.10.016

Ollivier-Gooch, C. (2003). A toolkit for numerical simulation of PDE's I: Fundamentals of generic finite-volume simulation. Journal of Computational Physics, 192(1), 1147–1175. https://doi.org/10.1016/S0021-9991(03)00335-5

Oliveira, F. S. (2013). Estudo de materiais para fabricação de bocais de motor de foguete a propelente híbrido [Master's thesis, Universidade de Brasília]. UnB.

Radtke, J. J. (2014). Otimização da geometria da seção divergente de tubeiras de motores-foguete [Master's thesis, Universidade Federal do Paraná]. UFPR.

Rao, G. V. R. (1958). Exhaust nozzle contour for optimum thrust. Journal of Jet Propulsion, 28(6), 377–382. https://doi.org/10.2514/8.7324

Roe, P. L. (1981). Approximate Riemann solvers, parameter vectors, and difference schemes. Journal of Computational Physics, 43(2), 357–372. https://doi.org/10.1016/0021-9991(81)90128-5

Sutton, G. P., & Biblarz, O. (2016). Rocket propulsion elements: An introduction to the engineering of rockets (9th ed.). Wiley. (Original work published 2000)

Taillandier, J. (2006). Efeito do modelo matemático sobre a solução numérica do escoamento em tubeira de motor foguete [Bachelor's thesis, Universidade Federal do Paraná]. UFPR.

Titarev, V. A., Tsoutsanis, P., & Drikakis, D. (2010). WENO schemes for mixed-element unstructured meshes. Communications in Computational Physics, 8(3), 585–609. https://doi.org/10.4208/cicp.2009.09.184

Toro, E. F. (2009). Riemann solvers and numerical methods for fluid dynamics: A practical introduction (3rd ed.). Springer. https://doi.org/10.1007/b79761

Tu, J., Yeoh, G. H., & Liu, C. (2018). Computational fluid dynamics: A practical approach (3rd ed.). Butterworth-Heinemann.

van Leer, B. (2003). Upwind and high-resolution methods for compressible flow: From donor cell to residual-distribution schemes. In 41st AIAA Aerospace Sciences Meeting and Exhibit. AIAA. https://doi.org/10.2514/6.2003-3559